



This is a repository copy of *Investigating deformation and failure mechanisms of discontinuous anti-dip bench rock slopes through shaking table tests and numerical simulations*.

White Rose Research Online URL for this paper:

<https://eprints.whiterose.ac.uk/226341/>

Version: Published Version

Article:

Yang, F., Xin, C., Wang, Z. orcid.org/0000-0002-4054-0533 et al. (3 more authors) (2025) Investigating deformation and failure mechanisms of discontinuous anti-dip bench rock slopes through shaking table tests and numerical simulations. *Rock Mechanics and Rock Engineering*, 58 (5). pp. 5329-5361. ISSN 0723-2632

<https://doi.org/10.1007/s00603-024-04346-y>

Reuse

This article is distributed under the terms of the Creative Commons Attribution (CC BY) licence. This licence allows you to distribute, remix, tweak, and build upon the work, even commercially, as long as you credit the authors for the original work. More information and the full terms of the licence here:

<https://creativecommons.org/licenses/>

Takedown

If you consider content in White Rose Research Online to be in breach of UK law, please notify us by emailing eprints@whiterose.ac.uk including the URL of the record and the reason for the withdrawal request.



eprints@whiterose.ac.uk
<https://eprints.whiterose.ac.uk/>



Investigating Deformation and Failure Mechanisms of Discontinuous Anti-dip Bench Rock Slopes Through Shaking Table Tests and Numerical Simulations

Fei Yang¹ · Chunlei Xin^{1,2} · Zhao Wang³ · Xinyuan Yu⁴ · Wenkai Feng¹ · Yunpeng Hu¹

Received: 25 May 2024 / Accepted: 9 December 2024 / Published online: 29 January 2025
© The Author(s) 2025

Abstract

Large-scale shaking table tests and numerical simulations were conducted to investigate the deformation and failure mechanisms of an anti-dip bench rock slope with discontinuities. The study introduces the Displacement Baseline Offset Ratio (DBOR) to characterize the instability and failure processes of slopes when they reach a plastic state under seismic excitations. It examines the peak ground displacement and earth pressure responses, as well as the cumulative damage processes of the slope model to provide insight into the deformation and failure mechanisms. The results show a significant displacement amplification effect at elevated points of the slope when subjected to seismic excitations. Furthermore, as the input frequency of the sine wave increases, the amplitude of the displacement response at the upper part of the slope accelerates. The widest bench divides the entire slope into smaller segments, hindering the deformation and failure across the benches and reducing stress transfer from the upper slope, thereby preventing stress concentration at the toe of the slope. The distribution of DBOR suggests that plastic deformation is more pronounced on the inner side of the bench than on the outer side, leading to earlier cracking on the inner side. A critical displacement threshold for seismic damage of each bench is established based on residual displacement responses and critical peak acceleration. These findings provide theoretical references for the risk assessment and seismic design of bench rock slopes.

Highlights

- Developed the Displacement Baseline Offset Ratio to measure slope instability under seismic forces.
- Significant displacement increases were found at higher slope points, intensified by higher seismic frequencies.
- Wide benches segment the slope, limiting deformation spread and reducing toe stress concentration.
- Established displacement limits for seismic damage, aiding slope risk assessment.
- Low frequencies cause overall deformation, while high frequencies lead to localized sliding failures.

Keywords Anti-dip bench rock slope · Baseline offset ratio offset · Shaking table test · Numerical simulation · Shattering failure mechanism

✉ Chunlei Xin
xinchunlei@cdut.edu.cn

✉ Zhao Wang
z.wang13@leeds.ac.uk

¹ State Key Laboratory of Geohazard Prevention and Geoenvironment Protection, Chengdu University of Technology, Chengdu, China

² College of Environment and Civil Engineering, Chengdu University of Technology, Chengdu, China

³ Institute for Transport Studies, University of Leeds, 34-40 University Rd, Leeds LS2 9JT, UK

⁴ School of Mechanical, Aerospace and Civil Engineering, The University of Sheffield, Sheffield, UK

1 Introduction

Western China, situated on the eastern edge of the Qinghai-Tibet Plateau, is riddled with extensive active faults. These faults contribute to numerous seismic zones across Southwest China, which have seen an increase in earthquake activity in recent years. Such earthquakes often trigger devastating geological disasters, such as landslides, collapses, and debris flows, resulting in significant loss of life and property damage (Che et al. 2016; He et al. 2021; Li et al. 2019). Among these, earthquake-induced landslides are the most destructive. Earthquakes also induce a type of secondary geological disaster, known as the “shattering slope”, which is characterized by its widespread distribution, latent threat, and large scale (He et al. 2020). This type of slope is prone to developing numerous seismic cracks that undermine the integrity of the rock mass, consequently reducing the slope's stability aftershocks and elevating the risk in regions susceptible to earthquakes. Existing fissures may widen, leading to the fragmentation of the slope into smaller blocks (Fan et al. 2017; Dong et al. 2021), which are destabilized by persistent gravitational forces, heightening the risk of collapse. Moreover, these cracks often act as channels for rainwater, which, when combined with aftershocks, can further erode the structural strength of the slope, leading to significant geological upheavals. (Cao et al. 2019). The magnitude of these disasters is underscored by events such as the 2008 Wenchuan earthquake. Within minutes of the main shock, the Wangjiayan landslide unleashed 1.4 million m³ of rock, devastating half a county and resulting in over 1700 fatalities. This event stands as one of the deadliest landslides triggered by the Wenchuan earthquake. Another significant event was the Guantan landslide, which occurred eight hours post-earthquake. This landslide moved 4.86 million m³ of material, creating a barrier lake that significantly threatened the safety of downstream residents. In 2010, heavy rainfall triggered a landslide in Suoqiao Village, Yanmen Township, known as the “shattering slope”. This landslide produced 17,000 m³ of debris and fully obstructed the G213 National Highway. Another major incident occurred in 2009 near the Chediguan Bridge, where a landslide dislodged over 10,000 m³ of rock and soil mass, demolishing the bridge piers and causing the entire 60-m-long bridge deck to collapse. This event resulted in six deaths and twelve injuries. These incidents underscore the importance of studying the seismic stability of complex rock slopes in geotechnical and seismic engineering.

Western China is experiencing significant infrastructure growth, including major highway and railway projects. Given the extremely complex geological conditions,

characterized by high mountains, deep gorges, and frequent seismic activity, bench slopes are often formed during road construction. Cutting these slopes into stepped shapes enhances their stability, reduces the overall slope angle, and guarantees road safety operation. Historically, anti-dip rock slopes are considered more stable than bedding rock slopes, with less likelihood of catastrophic failure during earthquakes (Chen et al. 2020a; Chen et al. 2020b; Dang et al. 2022; Fan et al. 2019). However, research on anti-dip rock slopes, particularly those formed as bench slopes during earthquakes, is still relatively limited. Addressing this research gap is crucial for understanding the shattering damage mechanism and instability characteristics of anti-dip bench rock slopes under earthquake excitations. At present, field investigations, shaking table tests, and numerical simulations are often used to study the dynamic response law and instability failure process of slopes under earthquake excitations (Peng et al. 2019; Song et al. 2020; Song et al. 2021a, b; Xu et al. 2018; Yin et al. 2010). Numerical simulation methods, such as the finite element method (FEM), discrete element method (DEM), finite difference method (FDM), and discontinuous deformation method (DDA), are widely utilized to study the dynamic response of various geological structures, including bedding slopes, anti-dip slopes, and block slopes in rock slopes (Song et al. 2019). However, limitations in the numerical model, including mesh size, boundary conditions, initial conditions, and parameter selection, can significantly affect the simulated results of slope dynamic response. In contrast, shaking table tests offer more precise control over parameters that mirror actual situations, including model size, ground motion input parameters, and boundary conditions, making them a preferred method for investigating the dynamic response and instability failure processes of slopes (Chen et al. 2020b; Dong, et al. 2022; Wu et al. 2020a, b). Researchers have distinguished the dynamic responses between bedding and anti-dip slopes by examining acceleration amplification effects, slope surface displacement, and marginal spectrum (Fan et al. 2016; Song et al. 2021a, b). The seismic cumulative failure effect on the slope with complex geological structure has been studied by considering plastic deformation characteristics, where low-frequency components have a controlling effect on overall stability, and high-frequency components have a significant impact on the accumulation process of local slope deformation (Song et al. 2021a, b). Additionally, the seismic behavior of slopes has been assessed through field investigations and large-scale shaking table tests by analyzing the evolution relationship between dynamic stress and strain, defining the critical state of slope instability (Tao et al. 2023a; Zhang et al. 2022). Notably, the acceleration amplification factor

near fissures during peak ground acceleration significantly exceeds that in non-fissured slopes. This discrepancy results in stress concentrations in the middle and upper parts adjacent to the fissure (Tao et al. 2023b; Tao and Dang 2023; Wu et al. 2020a, b).

Bench rock slopes with discontinuities tend to fail gradually under seismic excitations, rather than abrupt failure (Dong et al. 2022; Zhou et al. 2022). The deformation and failure of these slopes are influenced by the physical and mechanical properties of the rock mass and the discontinuities, along with their geometric distribution. Typically, local deformations occur first, once these deformations accumulate to a certain extent, they lead to an overall sliding failure of the slope (Qi et al. 2022). However, many previous studies have predominantly emphasized acceleration, displacement, and earth pressure in their exploration of the dynamic response of slopes, without considering residual deformations (Ning et al. 2019; Pu et al. 2020; Dong et al. 2020; Su et al. 2021). To offer a more detailed understanding of the progressive failure process of slopes under seismic excitations, this paper introduces the displacement baseline offset ratio (DBOR). DBOR assesses the deformation and collapse process of slopes, focusing on residual deformations after slopes reach a plastic state. Displacements are measured using sensors and non-contact photography techniques, generating displacement time-history curves at various locations on the bench rock slope. These displacement signals are then decomposed into sub-signals of varying frequencies through wavelet transform. By selecting the low-scale wavelet coefficients, the baseline of the displacement time-history curves is derived, revealing the residual deformation of the slopes. This analysis of deformation responses serves as a pivotal indicator for gauging the deformation and failure process of rock mass structures under seismic excitations. Such insights

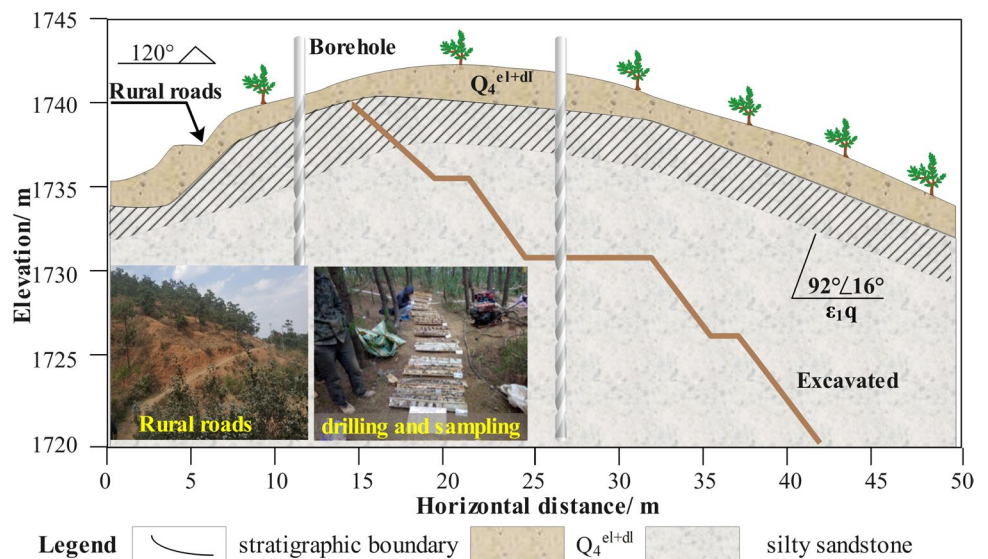
can be widely used for slope monitoring and early warning, aiming to reduce casualties and property losses caused by landslides.

This study employed both large-scale shaking table tests and numerical simulations to investigate the deformation and failure mechanisms of anti-dip bench rock slopes. The experimental setup modeled a scaled-down slope on a shaking table, designed to mirror a full-scale slope found along the Sanqing Expressway in Yunnan, China. The slopes were excited with the Wenchuan earthquake wave and sine waves of different amplitudes and directions. The dynamic responses were analyzed, focusing on peak ground displacement, residual displacement, dynamic earth pressure, and the progressive failure process. In addition, this study advanced the understanding of plastic deformation by introducing the concept of DBOR as a method to assess the degree of plastic deformation of the slope during seismic excitations. Conclusions were drawn regarding the critical slope failure thresholds for each bench based on DBOR.

Table 1 The physical mechanical parameters of the prototype slope

Parameters	Density ρ (kg/m ³)	Elastic modulus E (MPa)	Cohesion c (KPa)	Internal friction angle φ (°)	Poisson's ratio μ
Rock mass	2250	780	493	36	0.32
Weak inter-layer	1950	94	77	25	0.36

Fig. 1 Geological section and site photographs of the study area



2 Experiment Setup and System Calibration

2.1 Overview of the Slope

The study area is located in northwestern Yunnan Province, China, notable for its significant topographical diversity. The slope in this area has a natural dip angle of approximately 26° (as shown in Fig. 1). The construction of a highway through this area has led to the modification of the slope into a bench slope, thereby enhancing its stability. Borehole sampling results reveal that the bench slope is primarily composed of fully weathered silty sandstone, which has significantly compromised the integrity of the original rock structure, making it soft. The maximum recorded thickness of this exposed layer is 51.7 m. The rock mass displays a layered structure characterized by prevalent joints and fissures. The core is mostly broken into blocks ranging in diameter from 2 to 8 cm. The joint length is 5–8 cm. The physical and mechanical parameters of the rock mass are detailed in Table 1 (Xin et al. 2024).

According to the regional geological survey, the roadbed lies on the eastern branch of the Xiaojiang Fault, which is an active fault in the Holocene that intersects with the road, placing it in a geologically unstable area. The presence of well-developed joints and fissures is notable, with one group observed (J1: $258^\circ \angle 77^\circ$, and 2–3 pieces/m). The occurrence of the rock layer is $92^\circ \angle 16^\circ$, featuring a smooth surface filled with viscous mineral particles. The rock strata are highly weathered and can be easily dislodged by hammering. The interlayer spacing measures approximately 3–4 cm. After excavation, the geological structure of the slope is revealed as an anti-dip layered rock mass with a dip angle of 16° . This geological structure of the slope is shown in Fig. 1. Yunnan Province, located between the Eurasian Plate and the Indian Ocean Plate, is characterized by numerous active fault zones and a history of frequent earthquakes. From 2012 to 2020, the region experienced 592 earthquakes with magnitudes exceeding 2.0 on the Richter scale. Given the frequency of these seismic activities and the challenging geological landscape, there is an imperative need to understand the deformation and failure mechanisms of anti-dip bench rock slopes under seismic excitations.

2.2 Shaking Table Performance Testing

This series of experiments was conducted at the State Key Laboratory of Geohazard Prevention and Geoenvironment Protection at Chengdu University of Technology. The platform has dimensions of 4 m \times 6 m and a maximum load capacity of 4×10^4 kg. The motion of the shaking table is controlled by eight actuators, which allow for three-directions six-degree-of-freedom motion, including both

translational and rotational motions along the X/Y/Z axes (presented in Fig. 2a and b). The shaking table is hydraulically servo-controlled, and its main components include the platform, hydraulic system, loading system, servo valves and controllers, data acquisition system, and control software (see Fig. 2c). The main technical specifications and parameters of the shaking table are as follows: the operating frequency range is 0.1–60 Hz, and the maximum accelerations in the X, Y, and Z directions are 1.5 g, 1.2 g, and 1.0 g, respectively, corresponding to maximum displacements of 300 mm, 250 mm, and 150 mm.

The hydraulic shaking table involves multiple disciplines such as mechanics, hydraulics, infrastructure, and computer science, making it a complex system engineering project. The articulation stiffness and gap in the mechanical mechanism have a great influence on the uniformity of acceleration. For example, insufficient stiffness in the connecting part between the actuators and the platform, as well as friction and clearances in the connecting components, can cause waveform distortion. The stiffness of the shaking table foundation also has a significant impact on the accuracy of the input seismic waves. A low foundation stiffness can introduce anti-resonance peaks within the operating frequency range, reducing the system's bandwidth.

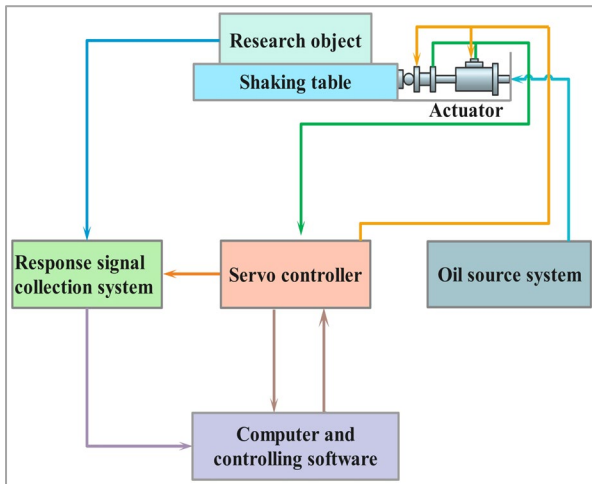
There is no unified standard for many performance indicators of the shaking table, and such standards are often only included in contracts by some manufacturers. However, the description of these indicators can be inconsistent. Thus, it is necessary to test the performance indicators of the shaking table so that the operational performance of the shaking table can accurately simulate earthquakes, thereby providing reliable experimental equipment for earthquake simulation shaking table tests. To evaluate the performance of the shaking table, nine accelerometers labeled A1 to A9 were strategically placed on the platform to study the performance curves for maximum displacement, maximum velocity, and maximum acceleration (presented in Fig. 2d). Additionally, the tests and analyses conducted included assessing the unevenness of acceleration, distortion of acceleration waveforms, and accuracy of seismic wave reproduction. During the testing of the maximum performance curve, a fixed-frequency sine wave was selected as the input waveform, with measurements taken in three sections along the curve.

To measure the maximum displacement, four frequencies were selected, starting from the lowest frequency and extending to the intersection point of displacement and velocity, with displacement amplitudes increasing gradually. This method was similarly applied to select frequency points for the maximum velocity and acceleration tests. The frequency range for the maximum displacement test spanned from 0.1 to 0.7 Hz. Actual test values for X-axis displacement consistently exceeded the expected performance value

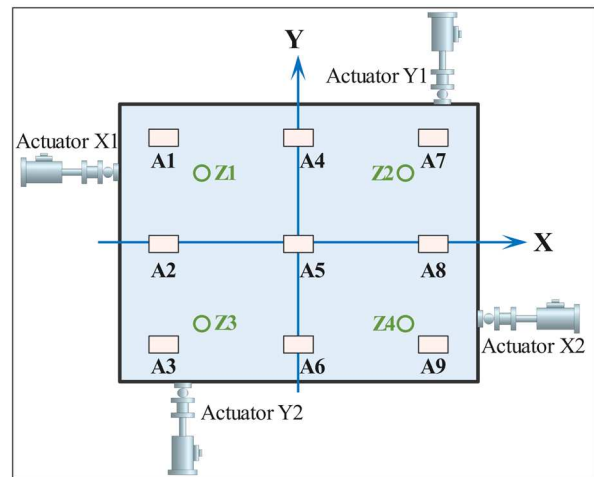


(a)

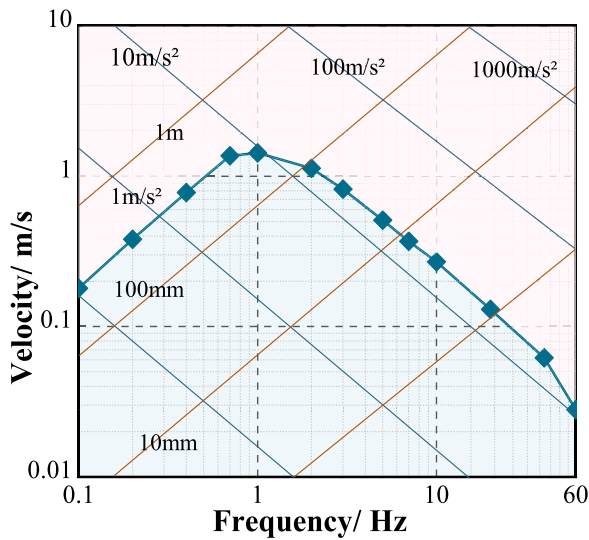
(b)



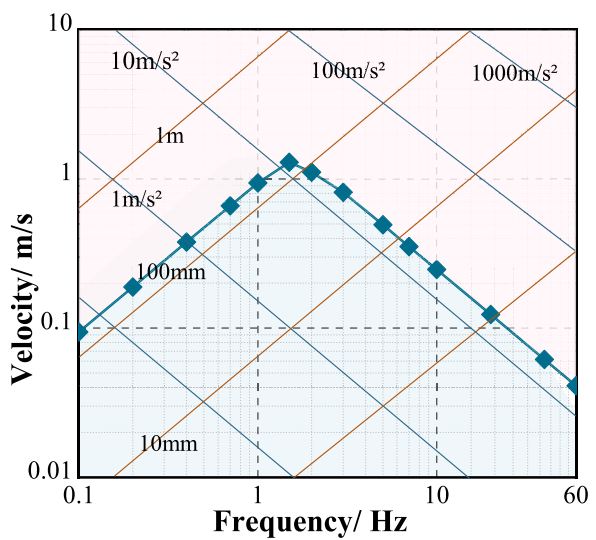
(c)



(d)



(e)



(f)

Fig. 2 The performance of the shaking table. **a** shaking table with three-direction six-degree-of-freedom motion; **b** the actuator; **c** main components of the shaking table; **d** monitoring point for the performance test; **e** maximum performance in the X direction; **f** maximum

performance in the Z direction; **g** displacement distortion of the shaking table; **h** acceleration distortion of the shaking table; **i** comparison of input and output waveform data; **j** correlation diagram between input and output waveform data

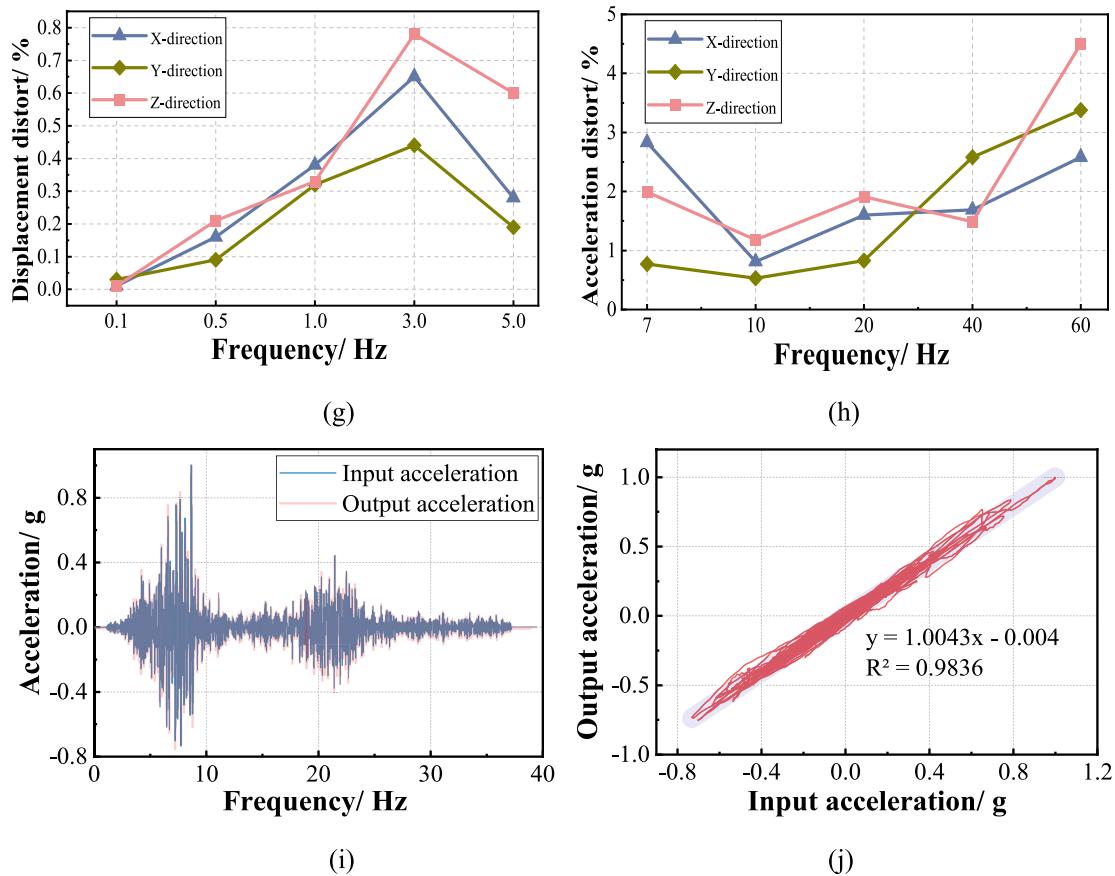


Fig. 2 (continued)

of 300 mm, and Z-axis displacement values surpassed the anticipated 150 mm. For the maximum velocity test, the frequency range was set between 1.0 and 2.0 Hz. Here, actual test values for the X-axis velocity exceeded the expected 1.2 m/s, and those for the Z-axis velocity were above the forecasted of 1.0 m/s. The frequency range for the maximum acceleration test covered 5–60 Hz. In this range, actual test values for X-axis acceleration exceeded the predicted 15 m/s^2 , and Z-axis values surpassed the anticipated 10 m/s^2 . The resulting maximum performance curves for the X and Z directions are illustrated in Fig. 2e and f. To evaluate displacement distortion of the platform, sine waves at frequencies of 0.1, 0.5, 1, 3, and 5 Hz were employed, with the calculation formula provided in Formula (1), where D_1 represents the fundamental wave amplitude of the displacement spectrum, and D_i represents the harmonic wave amplitude of the displacement spectrum. Testing confirmed that the maximum displacement distortion stayed within 3% for each degree of freedom of the system in sinusoidal vibrations below 5 Hz. Figure 2g presents the displacement distortion in the X, Y, and Z directions.

$$d = \frac{\sqrt{\sum_{i=2}^n D_i^2}}{D_1} \quad (1)$$

To assess the acceleration distortion of the shaking table, sine waves at frequencies of 7, 10, 20, 40, and 60 Hz were used during testing in acceleration-controlling mode. The amplitudes of both the fundamental and harmonic waves were measured using Fast Fourier Transform analysis. The calculation formula, shown in Formula (1), defines D_1 as the fundamental wave amplitude of the acceleration spectrum, and D_i as the harmonic wave amplitude of the acceleration spectrum. Test results indicate that the acceleration distortion in the X, Y, and Z directions is less than 5%, and this distortion is depicted in Fig. 2h. Further, the dynamic response of the platform was evaluated by iteratively controlling the input of actual seismic waves from typical seismic stations and collecting the waveform data of the output seismic waves from the shaking table. This process assessed the accuracy of seismic wave simulation. The coherence coefficient, a dimensionless quantity, was used to study the degree of linear correlation between variables. When two

random variables X and Y are independent, the correlation coefficient can be determined using Formula (2).

$$\rho_{XY} = \frac{Cov(X, Y)}{\sqrt{D(X)}\sqrt{D(Y)}} \tag{2}$$

The waveform data collected from the shaking table are compared with the original input waveform data, as shown in the time-history curve in Fig. 2i. The correlation diagram, shown in Fig. 2j, uses the input waveform as the horizontal axis and the output waveform as the vertical axis.

2.3 Similarity Design and Material Selection

Maintaining similarity between the prototype and the model slope is crucial in shaking table tests. Establishing a similarity relationship ensures that the physical and mechanical parameters of the prototype and the model maintain the same dimensions, differing only in scale. Therefore, the physical phenomena and failure processes observed in the test exhibit the same fundamental characteristics, allowing for the study of the dynamic response of the prototype slope. However, due to limitations in experimental materials and techniques, achieving complete similarity between the model and the prototype in shaking table tests can often be challenging (Xin, et al. 2018). Consequently, this experiment prioritized the following selected indicators to maintain geometric, kinematic, and dynamic similarity with the prototype parameters. When two physical phenomena exhibit these three types of similarity, they are considered congruent. To mitigate scale effects and ensure the scalability of results from model tests, several key measures have been implemented. A larger geometric similarity ratio of 25 was chosen for the physical simulation experiments to minimize the influence of scale effects on the outcomes. Flexible materials, such

as polystyrene foam boards, were utilized within the model box to absorb seismic waves, significantly reducing wave reflection and the resultant errors. This strategy effectively diminishes the influence of boundary conditions, allowing the model material to deform similarly to the prototype in a free field under seismic excitation, thus better approximating actual engineering conditions. Additionally, sensors are strategically positioned at a certain distance from the model boundaries to minimize the impact of boundary effects on the experimental results, particularly in mitigating the influence on internal shear strain measurements.

In this experiment, the anti-dip bench rock slope is characterized by 14 independent physical quantities, including geometric dimensions, gravitational acceleration, density, elastic modulus, Poisson's ratio, cohesion force, internal friction angle, stress, strain, time, displacement, damping ratio, frequency, and velocity. Three main controlling indicators, length (*L*), density (*ρ*), and acceleration (*a*), were selected. The remaining 11 physical quantities are derived variables according to the Buckingham π theorem. Each of these quantities possesses distinct dimensions, ensuring that the dimensions of each term within any physical equation remain homogeneous. Thus, these 11 physical quantities can be expressed as a functional relationship between the similarity criteria π₁, π₂, ..., π₁₁, as shown in Eq. (3) and Eq. (4). Substituting the dimensions corresponding to each physical quantity into Eq. (5) yields Eq. (6). This facilitates solving for the algebraic relationships among the parameters, culminating in Eq. (7). Given the presence of 14 unknown variables against only 4 equations, the dimensional coefficients for the 11 derived physical quantities are systematically organized in a table following the sequence of π₁, π₂, ..., π₁₁, then the similarity criteria are solved. The similarity relationships and ratios pertinent to the experiment are detailed in Table 2.

Table 2 The similarity criterion based on the matrix method and similarity ratios

	<i>E</i>	<i>μ</i>	<i>c</i>	<i>φ</i>	<i>σ</i>	<i>ε</i>	<i>t</i>	<i>d</i>	<i>ν</i>	<i>f</i>	<i>ξ</i>	<i>l</i>	<i>a</i>	<i>ρ</i>	Equation	Similarity criterion	Similarity ratios
	<i>a</i> ₄	<i>a</i> ₅	<i>a</i> ₆	<i>a</i> ₇	<i>a</i> ₈	<i>a</i> ₉	<i>a</i> ₁₀	<i>a</i> ₁₁	<i>a</i> ₁₂	<i>a</i> ₁₃	<i>a</i> ₁₄	<i>a</i> ₁	<i>a</i> ₂	<i>a</i> ₃			
π ₁	1	0	0	0	0	0	0	0	0	0	0	-1	-1	-1	π ₁ = <i>E</i> /(<i>lρa</i>)	<i>C</i> _{<i>E</i>} = <i>C</i> _{<i>l</i>} <i>C</i> _{<i>ρ</i>} <i>C</i> _{<i>a</i>}	<i>C</i> _{<i>E</i>} =25
π ₂		1	0	0	0	0	0	0	0	0	0	0	0	0	π ₂ = <i>μ</i>	1	<i>C</i> _{<i>μ</i>} =1
π ₃			1	0	0	0	0	0	0	0	0	-1	-1	-1	π ₃ = <i>c</i> /(<i>lρa</i>)	<i>C</i> _{<i>c</i>} = <i>C</i> _{<i>l</i>} <i>C</i> _{<i>ρ</i>} <i>C</i> _{<i>a</i>}	<i>C</i> _{<i>c</i>} =25
π ₄				1	0	0	0	0	0	0	0	0	0	0	π ₄ = <i>φ</i>	1	<i>C</i> _{<i>φ</i>} =1
π ₅					1	0	0	0	0	0	0	-1	-1	-1	π ₅ = <i>σ</i> /(<i>lρa</i>)	<i>C</i> _{<i>σ</i>} = <i>C</i> _{<i>l</i>} <i>C</i> _{<i>ρ</i>} <i>C</i> _{<i>a</i>}	<i>C</i> _{<i>σ</i>} =25
π ₆						1	0	0	0	0	0	0	0	0	π ₆ = <i>ε</i>	1	<i>C</i> _{<i>ε</i>} =1
π ₇							1	0	0	0	0	-1/2	-1/2	0	π ₇ = <i>t</i> /(<i>a</i> / <i>l</i>) ^{1/2}	<i>C</i> _{<i>t</i>} = <i>C</i> _{<i>l</i>} ^{1/2} <i>C</i> _{<i>a</i>} ^{-1/2}	<i>C</i> _{<i>t</i>} =5
π ₈								1	0	0	0	-1	0	0	π ₈ = <i>d</i> / <i>l</i>	<i>C</i> _{<i>d</i>} = <i>C</i> _{<i>l</i>}	<i>C</i> _{<i>d</i>} =25
π ₉									1	0	0	-1/2	-1/2	0	π ₉ = <i>v</i> /(<i>a</i> / <i>l</i>) ^{1/2}	<i>C</i> _{<i>v</i>} = <i>C</i> _{<i>l</i>} ^{1/2} <i>C</i> _{<i>a</i>} ^{1/2}	<i>C</i> _{<i>v</i>} =5
π ₁₀										1	0	1/2	-1/2	0	π ₁₀ = <i>f</i> /(<i>a</i> / <i>l</i>) ^{1/2}	<i>C</i> _{<i>f</i>} = <i>C</i> _{<i>l</i>} ^{-1/2} <i>C</i> _{<i>a</i>} ^{1/2}	<i>C</i> _{<i>f</i>} =1/5
π ₁₁											1	0	0	0	π ₁₁ = <i>ξ</i>	1	<i>C</i> _{<i>ξ</i>} =1

$$F(\pi_1, \pi_2, \pi_3 \dots \pi_{11}) = 0 \quad (3)$$

$$f(l, a, \rho, E, \mu, c, \varphi, \sigma, \varepsilon, t, d, v, f, \xi) = 0 \quad (4)$$

$$\pi_i = [l]^{a_1} \cdot [a]^{a_2} \cdot [\rho]^{a_3} \cdot [E]^{a_4} \cdot [\mu]^{a_5} \cdot [c]^{a_6} \cdot [\varphi]^{a_7} \cdot [\sigma]^{a_8} \cdot [\varepsilon]^{a_9} \cdot [t]^{a_{10}} \cdot [d]^{a_{11}} \cdot [v]^{a_{12}} \cdot [f]^{a_{13}} \cdot [\xi]^{a_{14}} \quad (5)$$

$$M^0 L^0 T^0 = L^{a_1} \cdot (LT^{-2})^{a_2} \cdot (ML^{-3})^{a_3} \cdot (ML^{-1}T^{-2})^{a_4} \cdot (1)^{a_5} \cdot (ML^{-1}T^{-2})^{a_6} \cdot (1)^{a_7} \cdot (ML^{-1}T^{-2})^{a_8} \cdot (1)^{a_9} \cdot (T)^{a_{10}} \cdot (L)^{a_{11}} \cdot (LT^{-1})^{a_{12}} \cdot (T^{-1})^{a_{13}} \cdot (1)^{a_{14}} \quad (6)$$

$$\begin{cases} a_1 + a_2 - 3a_3 - a_4 - a_6 - a_8 + a_{11} + a_{12} = 0 \\ -2a_2 - 2a_4 - 2a_6 - 2a_8 + a_{10} - a_{12} - a_{13} = 0 \\ a_3 + a_4 + a_6 + a_8 = 0 \\ a_5 + a_7 + a_9 + a_{14} = \text{constant} \end{cases} \quad (7)$$

Similarity materials were used in this experiment to accurately represent the rock mass and the weak interlayer. The target values for each physical and mechanical parameter of the model material were calculated based on the established similarity relationships. Similarity materials were used to represent the rock mass, consisting of a mixture of barite powder, bentonite, gypsum, paraffin oil, and water. In this mixture, barite powder served as the aggregate, gypsum acted as the binding agent, and paraffin oil functioned as a water retainer. To simulate the characteristics of a weak interlayer with low strength and low elastic modulus, a mixture of bentonite and paraffin oil was prepared. After repeated adjustments of the proportions and conducting various tests—including direct shear tests, uniaxial compression tests, triaxial compression tests, and ring knife tests—the cohesion, internal friction angle, elastic modulus, and density of the simulated materials were accurately measured. The final proportions for the rock mass material were set using the following ratios: barite powder to bentonite to gypsum to paraffin oil to water at 65:13:5:13:3. For the weak interlayer, the ratio of bentonite to paraffin oil was established at 25:2. Details of these materials and the results of their physical and mechanical property tests are displayed in Fig. 3, while the physical and mechanical parameters of the model slope are documented in Table 3.

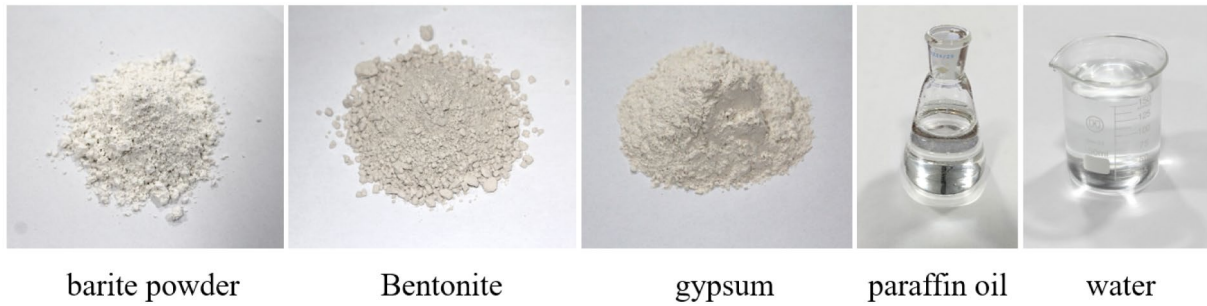
2.4 Design and Preparation of the Model Slope

The prototype slope under examination is a three-bench slope in a road cutting, with each bench standing at a height of 5 m. The first and third benches have a width of 2 m, while the second bench measures 8 m in width. Adhering to a geometric similarity ratio of 25, the model slope designed for the shaking table test features each bench at a height of 20 cm, the widths of the first and third benches are 8 cm, and

the second bench is 32 cm. The weak interlayer is incorporated with a thickness of 0.5 cm and an inclination angle of 16°. To analyze the dynamic response and progressive failure phenomena of the bench slope, a variety of instruments were utilized, including accelerometers, earth pressure cells, displacement sensors, digital image correlation (DIC), and cameras. Specifically, the monitoring cross-section of the slope model, representing the central section of the slope, is indicated with a red dashed line, as shown in Fig. 4a. Sensors were strategically placed at the transition points of slope gradients on the surface, where the highest stress concentrations were anticipated based on preliminary finite element analysis and previous experimental data. Additionally, accelerometers were distributed at varying heights of the slope, providing a comprehensive view of the deformation patterns. Given the inner sides of the benches are potential failure zones, earth pressure cells were placed at these positions. Figure 4b provides a detailed depiction of the specific locations and numbers of the sensors.

Each sensor was calibrated before the experiment to ensure data reliability. Instruments were strategically placed: accelerometers, earth pressure cells, and displacement sensors were embedded on the surface of each bench. Additional accelerometers were buried at various monitoring locations within the slope to record its dynamic response characteristics. The accelerometers adopted were IEPE piezoelectric type 1A314E series, with axial sensitivities in the X, Y, and Z directions of $10 \pm 0.5 \text{ mV/m}\cdot\text{s}^{-2}$ and a measurement range of $\pm 50 \text{ g}$. The earth pressure cells had a model number of BW with a measurement range of 1 MPa, a sensitivity of 5 mV/MPa, and a diameter of 28 mm. The displacement sensors were MIRAN KTR11 rebound displacement sensors, offering a sensitivity and accuracy of 0.01 mm. These sensors were positioned on both the inner and outer sides of each bench to monitor the dynamic responses of each segment.

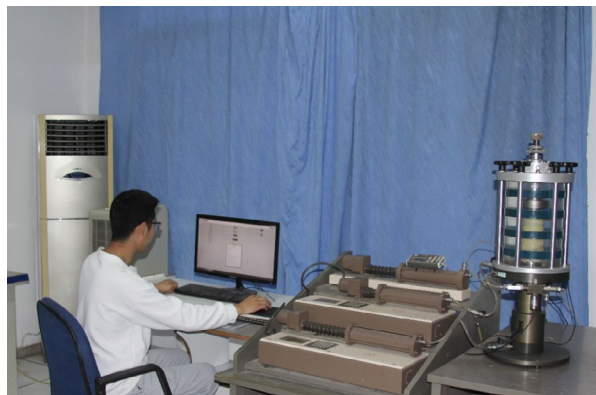
The construction of the slope model within the model container followed a systematic layer-by-layer compaction method from bottom to top, incorporating stacks of rock masses and weak interlayers as outlined by (Xin et al. 2019). This construction process comprises five distinct steps. Step 1: The outline of the slope and the position of the weak interlayers were marked on the acrylic plate of the model container to ensure that the model conformed to the design plan and maintained data reliability. Step 2: The mass of similar materials was calculated based on the geometric size and density of the slope. Materials were prepared according to the similarity ratio and mixed thoroughly using a small mixer. After mixing, the materials naturally bonded, forming clusters of coarse particles enveloped in dry material, which were then ground into fine particles using a 0.3 cm sieve. Step 3: The prepared mixture was placed into the model container using a volume control method to achieve the desired



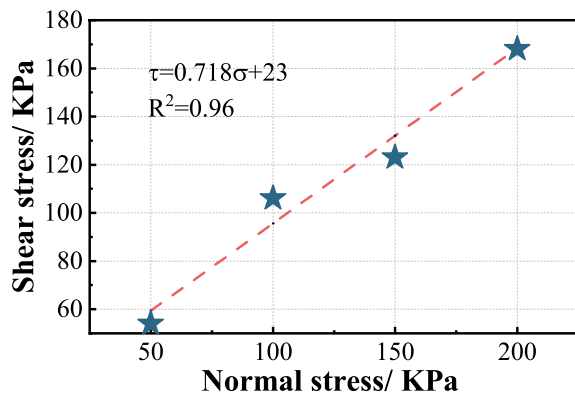
(a)



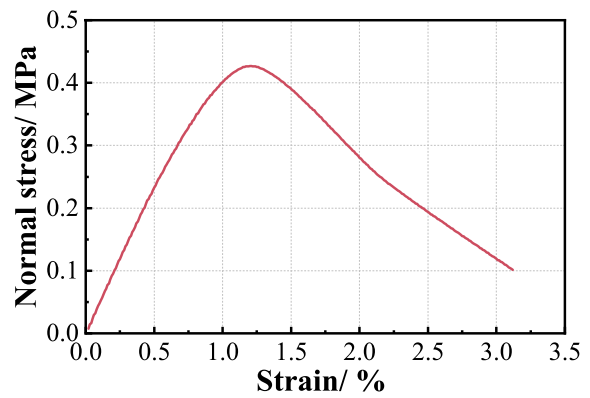
(b)



(c)



(d)



(e)

Fig. 3 Mechanical performance tests. **a** similarity materials; **b** direct shear test; **c** triaxial compression test; **d** shear stress-normal stress fitting curve for the direct shear test; **e** stress–strain curves under uniaxial compression

density through compaction. This method ensured adherence to the established similarity relationships and maintained a consistent compaction thickness of approximately 5 cm for each layer. The interlayer material was dyed red to facilitate the observation of dynamic responses and the failure processes during seismic activity. Step 4: Sensors were strategically installed at predetermined locations and calibrated to ensure precise data collection. Extra wire length was

to remain inside the slope to prevent any sensor damage from excessive tension due to compaction or potential sliding failures. Step 5: Speckle points were applied on the slope profile to assist in monitoring settlement deformation and instability failure. The entire process of slope construction is shown in Fig. 5.

Table 3 The physical mechanical parameters of the model slope

Parameters	Density ρ (kg/m ³)	Elastic modulus E (MPa)	Cohesion c (KPa)	Internal friction angle φ (°)	Poisson's ratio μ
Rock mass	2200	50	20	36	0.34
Weak inter-layer	1950	3.42	3	23	0.37

2.5 Seismic and Sine Wave Input Schemes for Dynamic Response Analysis

In this experiment, both the Wenchuan earthquake wave and sine wave were utilized as input waveforms to explore the dynamic response characteristics and instability failure modes of the anti-dip bench rock slope (Xin et al. 2020). The time history curves and Fourier spectra of these input waveforms are shown in Fig. 6a–d. Multiple-stage excitations were applied to the model slope to gather data for analyzing the dynamic response patterns prior to significant deformation and failure.

In addition, Fig. 6e displays the low-amplitude loading process, which employs both actual seismic waves and sinusoidal waves at varying frequencies. In the legend, WLX and WLXZ denote Wolong seismic waves loaded in the X and XZ directions, respectively. The sinusoidal waves are all loaded in the XZ direction. SIN3Hz specifies a sinusoidal wave frequency of 3 Hz, with similar notation for other frequencies. The loading amplitude gradually increases from 0.1 to 0.3 g. This setup helps explore the dynamic response changes of the bench rock slope under different low-amplitude excitations and provides insights into the elastic behavior of the slope under varied loading conditions. Figure 6f shows the high-amplitude loading process, with amplitudes ranging from 0.4 to 1.3 g. The purpose of the second loading stage is to examine the deformation and failure mechanisms of the bench rock when subjected to high-amplitude seismic waves, enabling a deeper analysis of the slope's stability and failure processes.

3 Results Analysis

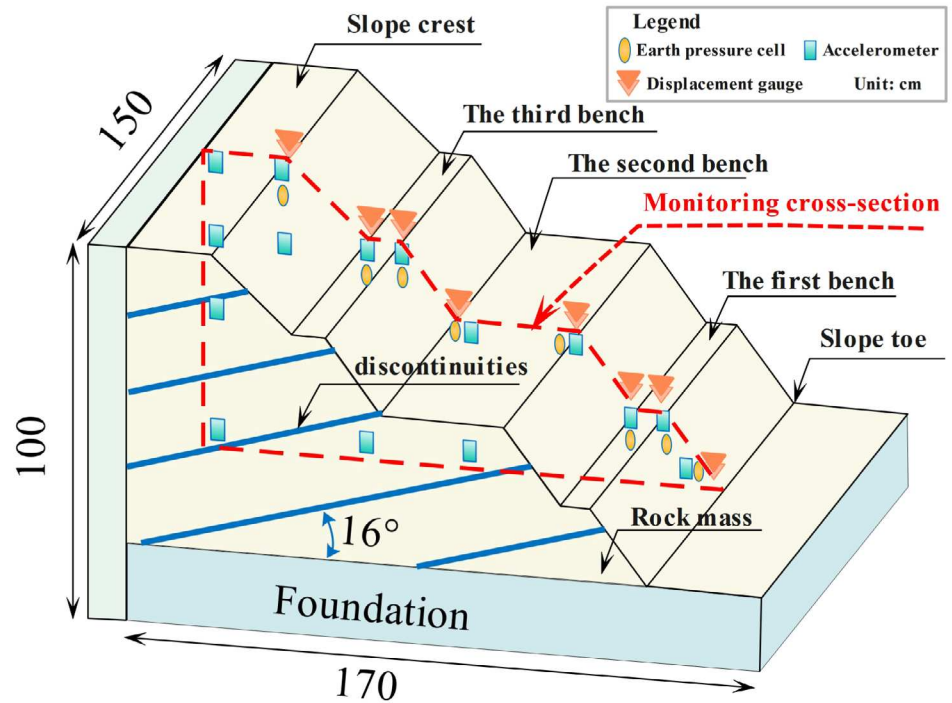
3.1 Dynamic and Residual Displacement Responses

Displacement sensors were strategically installed at various locations on the slope surface to continuously capture the displacement response of the slope in real time under seismic excitation. A comprehensive analysis of extensive displacement time-history data revealed that the baseline of

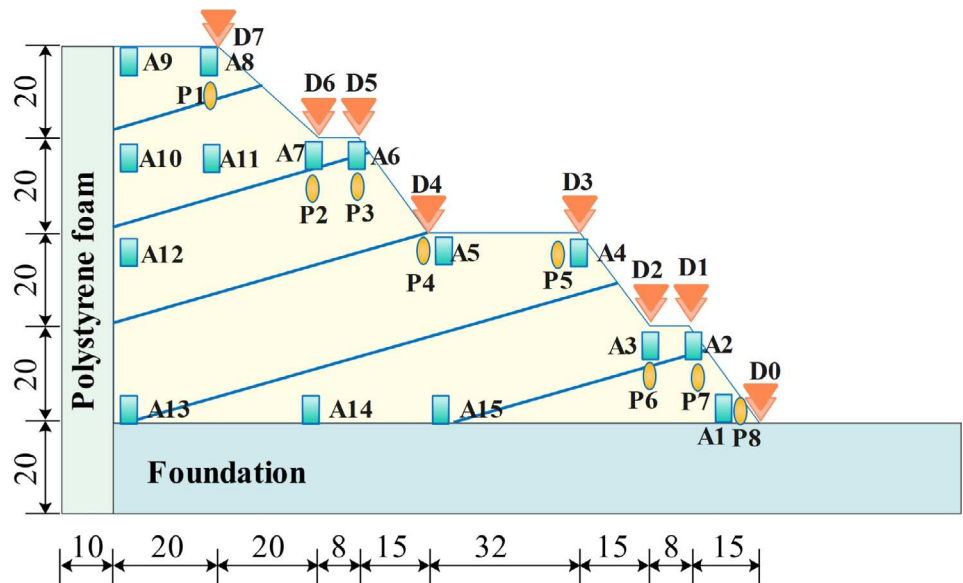
the displacement time-history at specific locations exhibited varying degrees of offset following multiple seismic events, signaling the presence of residual displacement within the slope. To analyze the dynamic response characteristics and instability failure process of the anti-dip bench rock slope, two important parameters were introduced: peak ground displacement (PGD) and residual displacement (RD). These parameters, as shown in Fig. 7a and b, are defined to reflect different dynamic behaviors of the slope under seismic excitations. Peak ground displacement and residual displacement have distinct physical interpretations. Peak ground displacement refers to the transient displacement that occurs on a slope during seismic excitation, which provides insights into the temporary deformation and response characteristics of slopes under such conditions. By analyzing peak ground displacement, the overall stability and deformation characteristics of slopes during seismic events can be studied. Conversely, residual displacement refers to the permanent displacement remaining on a slope after seismic excitation, serving as an indicator of enduring deformation. This metric is instrumental for conducting long-term stability and continuous deformation analysis of slopes. Furthermore, residual deformation is a vital metric commonly utilized in geological hazard evaluations to assess slope stability and issue early warnings. Peak ground displacement is the initial response under seismic excitation, indicating temporary deformation of the slope due to the seismic forces. If the peak ground displacement exceeds certain thresholds, it can lead to slope instability and eventual failure. In contrast, residual displacement develops gradually through multiple seismic excitations and does not appear until the end of seismic action. Analysis of extensive displacement time-history data reveals that both peak ground displacement and residual displacement of slopes increase with increasing peak ground acceleration of the input seismic waves. This underscores that the process of slope instability deformation is both gradual and cumulative.

Figure 7c and d show the peak ground displacement responses at monitoring points D1 and D5 on the slope surface under varying sine wave frequencies. As the input frequency of the sine wave increases, the amplitude of the peak ground displacement consistently rises. Specifically, at D1, when the input sine wave frequency is 10 Hz with an amplitude of 0.3 g, the peak ground displacement amplitude is 0.15 mm. This amplitude escalates to 0.81 mm when the frequency increases to 20 Hz, representing a 5.4-fold increase. In contrast, at monitoring point D5, a 10 Hz input sine wave with an amplitude of 0.3 g leads to a peak ground displacement amplitude of 0.4 mm, which dramatically increases to 4.1 mm at a frequency of 20 Hz, an increase by a factor of 10.25. This showcases a pronounced displacement amplification effect at higher elevations of the slope, where the displacement response in the upper part of

Fig. 4 Schematic diagram and monitoring points of the anti-dip bench rock slope



(a)



(b)

the slope significantly exceeds that in the lower part under identical frequency and amplitude sine waves. Moreover, this displacement response amplitude at the upper section of the slope accelerates more rapidly with increasing input frequency.

Figure 7e and f illustrate the peak displacement responses at various monitoring points on the slope surface, induced

by Wenchuan earthquake waves in the XZ and X directions, respectively. Initially, with low input peak ground accelerations, the displacement response across different positions on the slope is minimal. As the input peak ground acceleration increases, the displacement response also gradually increases. When the input acceleration peak exceeds 0.6 g, the displacement amplitude escalates rapidly. When



(a)



(b)



(c)



(d)



(e)



(f)

Fig. 5 Construction process of the model slopes. **a** outlining the slope and marking weak interlayer positions on the acrylic plate; **b** compacting the rock mass; **c** installing sensors;

d stacking weak interlayers; **e** applying marked points onto the acrylic plate; **f** completing construction of the anti-dip bench rock slope

the input peak ground acceleration reaches 0.6 g, the displacement response amplitudes on the outer side of the first, second, and third bench are 0.99 mm, 0.93 mm, and 1.34 mm, respectively. When the input peak ground acceleration increases to 0.9 g, the displacement amplitudes at these locations rise to 5.46 mm, 3.89 mm, and 6.08 mm, respectively, representing increases by factors of 4.52, 3.18, and 3.54. Among the benches, the second bench has the widest width, requiring a larger seismic inertial force to achieve the same level of displacement under seismic excitation as the narrower benches. Thus, the wider bench plays a role in mitigating the deformation and failure of the bench slope. For the same input peak ground acceleration, the displacement response varies with the loading direction. The displacement response in the XZ direction is larger than that in the X direction. Specifically, for the inner side of the second bench, when the input peak ground accelerations are 0.4 g, 0.6 g, 0.9 g, and 1.3 g, the displacement response in the XZ direction are 1.34, 1.81, 1.29, and 3.52 times larger than those in the X direction, respectively. This variability highlights the significant influence of loading direction on displacement response under seismic conditions.

Residual displacement is a key metric for assessing the post-earthquake stability of slopes. The Newmark method is another commonly used approach for analyzing the instability and failure of slopes under seismic excitations. Residual deformation, however, is a macroscopic behavior that manifests once a slope reaches its plastic state, with the instability and failure of the slope resulting from a combination of both dynamic and residual displacements. Post-earthquake field investigations have revealed that although some slopes may exhibit significant residual displacement responses, they may still retain their structural stability. Therefore it is not sufficient to fully characterize the degree of plastic damage to the slope. To quantify the instability and failure process of slopes after entering the plastic state, the displacement baseline offset ratio (DBOR) is employed, which takes into account both the peak ground displacement during the seismic excitation and the residual displacement after the seismic excitation, thereby offering a more comprehensive reflection of the plastic deformation behavior of the slope under the influence of seismic excitation.

The formula for calculating DBOR is presented in Eq. (8). The distribution of DBOR across various positions on the slope surface is shown in Fig. 8. This helps in understanding how different areas of the slope are affected by seismic forces and provides a detailed measure of potential instability and failure.

$$DBOR = \frac{RD}{PGD} \quad (8)$$

where RD represents residual displacement, PGD represents peak ground displacement.

Upon applying a peak ground acceleration of 0.4 g, the DBOR is most pronounced on the inner side of the second bench and the slope toe, indicating the initial entry into the plastic state at these locations under seismic excitation. This observation correlates with the initial onset of cracking at these parts, consistent with data collected on the phenomena of slope instability and failure (Bao et al. 2024; Chen et al. 2023; Fan et al. 2019; Shi et al. 2024; Zhou et al. 2022). As the input peak ground acceleration increases to 0.6 g, tensile failure occurs at the rear edge of the slope, where a pronounced DBOR is also observed. The contour map further reveals that the DBOR at the inner side of each bench is higher than at the outer side, indicating more significant plastic deformation and initial cracking at the inner sides under seismic excitation. With an input peak ground acceleration of 0.9 g, the highest DBOR values are observed at the rear edge of the slope and on the inner side of the second bench, with higher DBOR values at the upper part of the slope compared to the lower part. It can be seen from the slope profile that the second bench has the largest width, effectively dividing the complete slope into two sections and transforming the overall slope failure into local failure caused by the wider bench. At the input peak ground acceleration of 1.3 g, the DBOR dominates in the upper part of the slope, signifying it as the most vulnerable part of the slope. Under strong seismic excitation, this upper part of the slope experiences larger displacements due to elevation amplification effects. Continuous excitations lead to degradation in the mechanical properties of the rock mass, reducing its shear strength and resulting in the collapse of the slope surface and substantial deformations, with the upper part exhibiting a pronounced DBOR. Given the stepped surface of the slope, the inner sides of the benches experience stress concentration, making them more susceptible to cracking and deformation under seismic excitation. To assess the plastic deformation of these benches, the Damage-Based Offset Ratio (DBOR) of the inner sides is utilized. Figure 8e illustrates the distribution pattern of DBOR across the benches under various peak ground accelerations.

As the input peak acceleration increases, the plastic deformation of the slope shows an increasing trend, but the degree of deformation varies across different locations. To characterize the trend of DBOR, the difference in DBOR ($\Delta DBOR$) between successive stages of input peak ground acceleration was calculated. For example, the $\Delta DBOR$ for the 0.2~0.4 g range is obtained by subtracting the DBOR at 0.2 g from that at 0.4 g, as shown in Fig. 8f. Analysis of the $\Delta DBOR$ change patterns reveals that as the input peak acceleration increases, the plastic deformation of the bench slope initially increases and subsequently decreases. The “turning point” in $\Delta DBOR$ occurs when the input peak acceleration transitions from 0.6 g to 0.9 g. Therefore, the input peak acceleration of 0.6 g is identified as the “critical

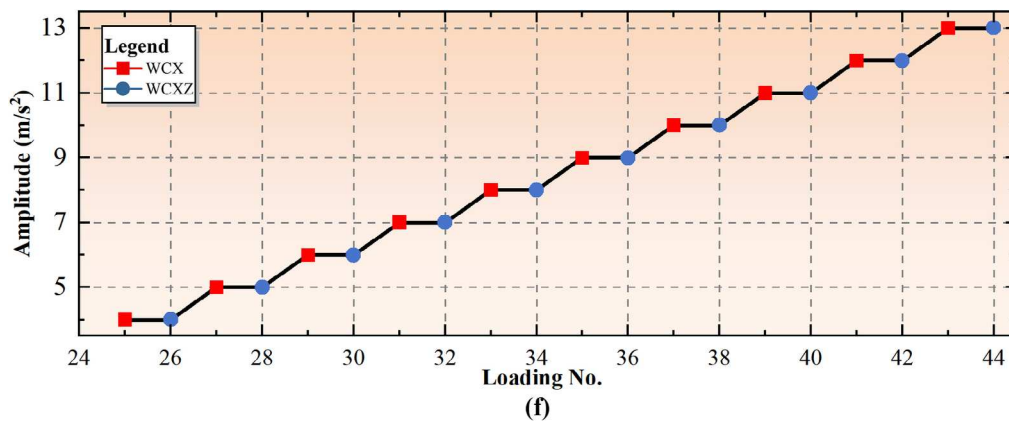
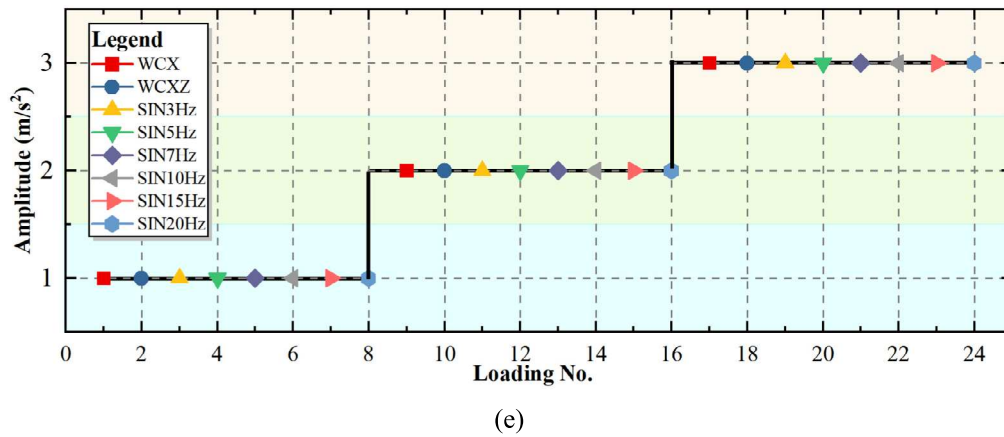
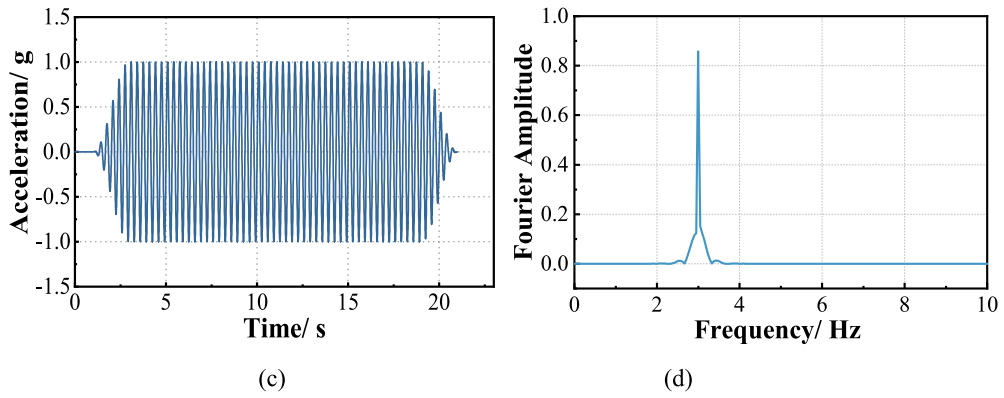
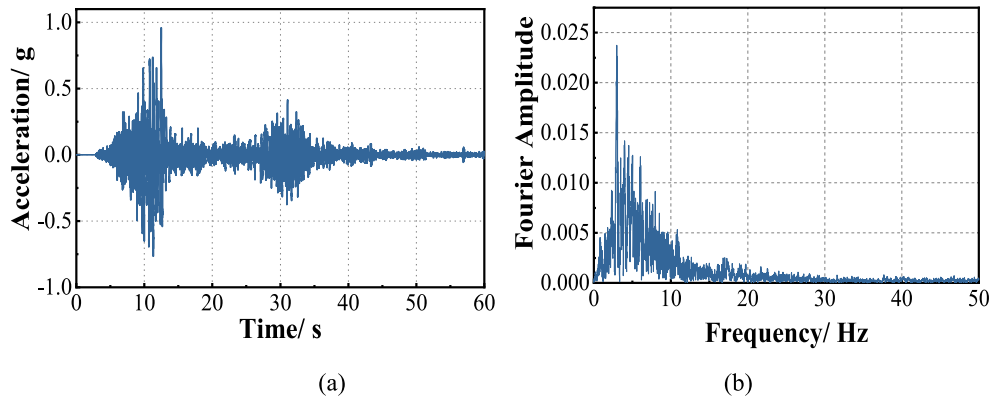


Fig. 6 The time history curves and Fourier spectra of the input waveform. **a** time history of the Wolong earthquake wave; **b** Fourier spectra of the Wolong earthquake wave; **c** time history of the sine wave with a frequency of 3 Hz; **d** Fourier spectra of the sine wave with a frequency of 3 Hz; **e** the low-amplitude loading process; **f** the high-amplitude loading process

acceleration” for initiating significant plastic damage in the slope. This critical value is further employed to estimate the threshold for cumulative permanent damage. Upon calculation, at 0.6 g input acceleration, the peak displacements for the first bench, second bench, third bench, and slope top are 0.985 mm, 0.614 mm, 1.13 mm, and 2.836 mm, respectively. Using the geometric similarity ratio derived from the experimental setup, these results are extrapolated to estimate the cumulative permanent damage thresholds for the prototype slope. For the anti-dip bench rock slope, the cumulative thresholds for permanent damage from the first bench to the slope top are determined to be 24.63 mm, 15.37 mm, 28.25 mm, and 70.94 mm. These thresholds are consistent with the California Geological Survey's benchmarks for shallow slope failure, which range from 0 to 150 mm (California Geological Survey, 2008).

3.2 Earth Pressure Responses

Stress variations and the distribution of post-earthquake stress, induced by seismic excitations, play critical roles in determining the deformation, failure mechanisms, and instability characteristics of slopes. These factors are pivotal in evaluating the post-earthquake stability of slopes. Figure 9a illustrates the variation of peak earth pressure at different benches of the slope under the excitation of the Wenchuan earthquake with varying peak ground accelerations. For monitoring points P1, P2, P6, and P7, the peak earth pressure increases with an increase in the input peak ground acceleration. Specifically, as the input peak ground acceleration rises from 0.4 to 0.6 g, the peak earth pressure at these monitoring points increases by 15.84%, 69.84%, 49.96%, and 26.81%. The increase in earth pressure is most pronounced at the base of the slope and least at the top. Under seismic excitations, the toe of the slope experiences compression from the overlying rock mass, resulting in larger shear stress and a rapid increase in earth pressure. However, for monitoring points P3, P4, P5, and P8, the peak earth pressure initially increases and then decreases as the input peak ground acceleration increases. This pattern reflects the deterioration of the mechanical properties of the rock mass under strong seismic excitations, leading to reduced shear strength. When this shear strength falls below a critical value, the slope reaches a critical state of cracking. With low input peak ground accelerations, the rock mass is subjected to

minimal stress, producing insignificant deformation and low peak earth pressure. As input peak ground acceleration increases beyond a specific threshold, the stress on the rock mass causes deformation and cracking, subsequently raising peak earth pressure. However, as the seismic acceleration continues to increase, the rock mass has already experienced failure and sliding, leading to a decrease in peak earth pressure.

Figures 9b and c display the distribution of peak earth pressure in the upper and lower parts of the slope under the action of a 0.3 g sine wave. It can be observed that as the input frequency of the sine wave increases from 3 to 15 Hz, the peak earth pressure continuously rises. However, when the input frequency further increases from 15 to 20 Hz, the peak earth pressure decreases. This indicates that the resonant frequency of the slope is approximately 15 Hz, which causes the maximum dynamic earth pressure responses at this frequency, resulting in the slope exhibiting a resonance phenomenon. The earth pressure on each bench in the lower part of the slope is higher than that on the upper part. For instance, with an input amplitude of 0.3 g and a frequency of 15 Hz sine wave, the earth pressure at P5 is 45.7 times that of P1, and at P6 is 5.89 times that of P2. As seismic waves propagate through the slope, they induce significant vibration and deformation in the rock mass. The lower part of the slope, constrained by the upper part, experiences stronger compression and shear forces during seismic excitations, resulting in higher dynamic earth pressures. Conversely, the lower benches of the slope, situated beneath the upper part, bear greater dynamic loads, resulting in a larger dynamic earth pressure response.

The variation in earth pressure between the outer and inner sides of each bench on the slope under different peak ground accelerations of the Wenchuan earthquake is depicted in Fig. 9d, e, and f. For the third bench, dynamic earth pressure on the inner side exceeds that on the outer side when the input peak ground acceleration ranges from 0.1 g to 0.3 g. During seismic excitations, the inner side of the bench experiences mutual compression from both the overlying rock mass and the outer side of the bench. Moreover, the inner side of the bench has stronger constraints compared to the outer side, resulting in higher dynamic earth pressure on the inner side. However, as the input peak ground acceleration increases from 0.4 g to 0.9 g, the dynamic earth pressure on the inner side of the bench becomes less than that on the outer side. This discrepancy occurs as the inner side of the bench gradually enters a plastic state, transforming into a tension zone. Meanwhile, the outer side of the bench undergoes significant deformation due to the strong seismic inertial forces and mutual compression of the rock mass, leading to higher dynamic earth pressure on the outer side compared to the inner side. For the second bench, the dynamic earth pressure

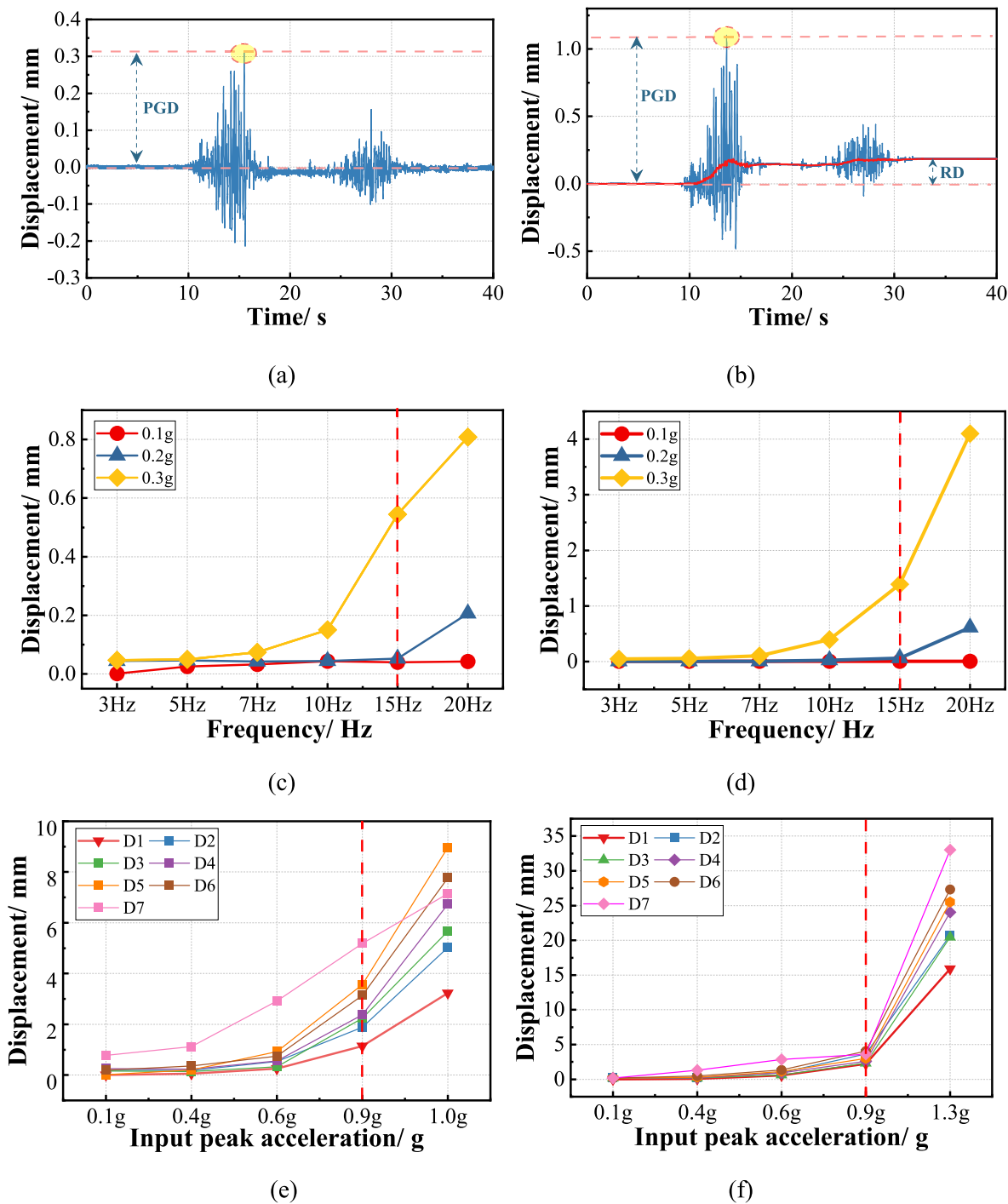


Fig. 7 The peak ground displacement response of the anti-dip bench rock slope. **a** displacement time-history curve at monitoring point D1 with 0.2 g peak ground acceleration; **b** displacement time-history curve at monitoring point D1 with 0.6 g peak ground acceleration; **c** peak ground displacement responses at monitoring point D1 to sine waves at varying frequencies; **d** peak ground displacement responses

at monitoring point D5 to sine waves at varying frequencies; **e** peak ground displacement responses at various monitoring points on the slope to the Wenchuan earthquake waves in the X direction; **f** peak ground displacement responses at various monitoring points on the slope to the Wenchuan earthquake waves in the XZ direction

on the inner side is consistently lower than on the outer side. Given its status as the widest of the three benches, the second bench effectively divides the entire slope into two smaller

slopes. This division reduces the stress transferred from the upper slope and mitigates stress concentration at the toe, thus mitigating adverse effects on the upper slope. Under seismic

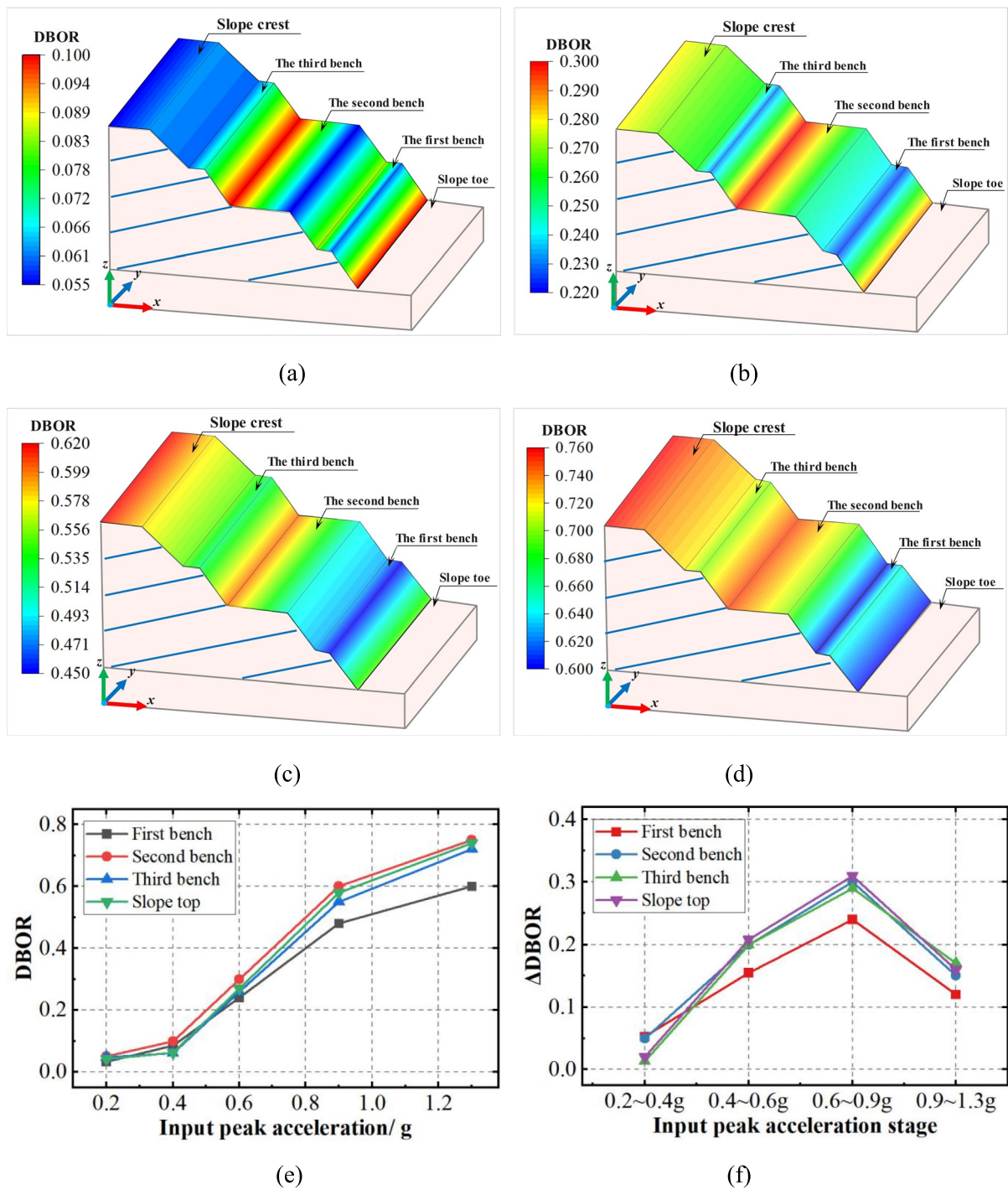


Fig. 8 The distribution of DBOR at various positions on the slope surface. **a** DBOR distribution with 0.4 g input peak ground acceleration; **b** DBOR distribution with 0.6 g input peak ground acceleration; **c** DBOR distribution with 0.9 g input peak ground acceleration;

d DBOR distribution with 1.3 g input peak ground acceleration; **e** the distribution pattern of DBOR for each bench under various peak ground accelerations; **f** the distribution pattern of Δ DBOR for each bench

excitations, the inner side of the second bench acts as the rear edge of the lower slope, becoming a focal area for tensile stress concentration and the initial site for crack formation. In contrast, the outer side, due to its larger width, experiences

less displacement but receives accumulated stress from the upper slope, resulting in higher dynamic earth pressure on the outer side. For the first bench, dynamic earth pressure is consistently higher on the inner side than on the outer side.

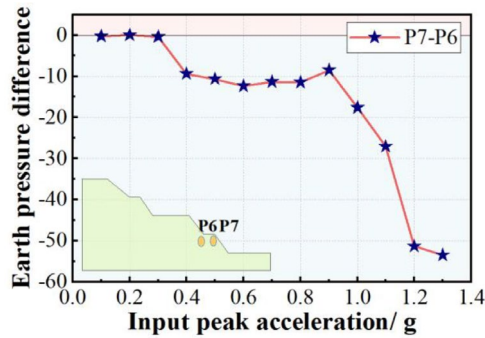
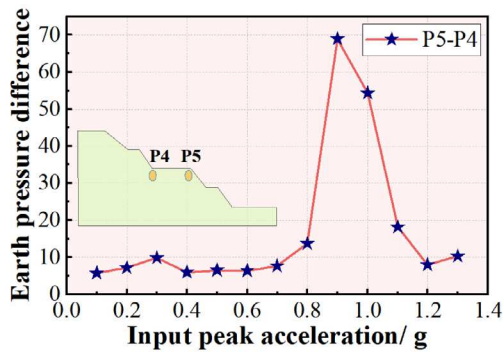
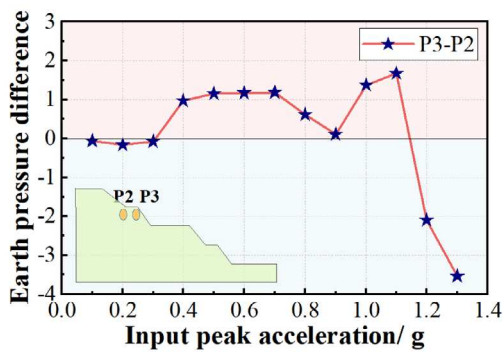
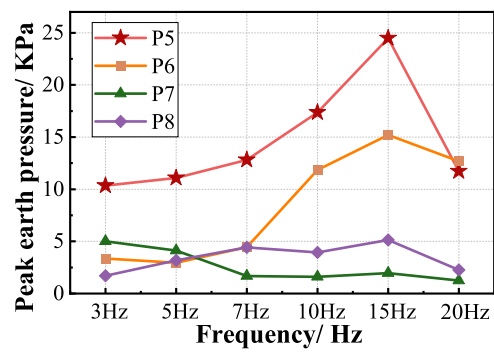
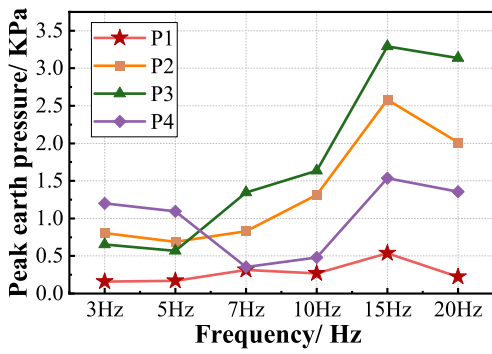
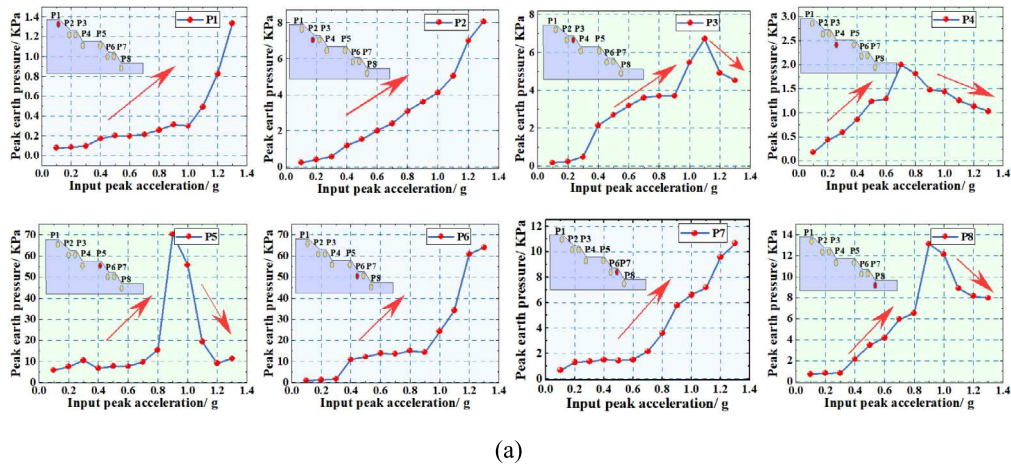


Fig. 9 The earth pressure responses on the slope. **a** peak earth pressure responses at various slope positions; **b** peak earth pressure distribution in the upper parts of the slope with loading amplitude of 0.3 g; **c** peak earth pressure distribution in the lower parts of the slope with loading amplitude of 0.3 g; **d** earth pressure difference between the outer and inner sides of the third bench; **e** earth pressure difference between the outer and inner sides of the second bench; **f** earth pressure difference between the outer and inner sides of the first bench

The stress from the upper slope is transmitted to the toe of the slope, intensifying stress concentration on the inner side of the first bench, which also displays bulging phenomena in the lower rock mass. The macro deformation and earth pressure distribution across each bench under seismic excitations can be categorized into translational displacement and rotational displacement, as shown in Fig. 10. For the second and third benches, the outer side of the bench undergoes rotational displacement around the inner side of the bench, resulting in lower dynamic earth pressure on the inner side. Conversely, the inner side of the first bench experiences rotational displacement around the outer side, leading to higher dynamic earth pressure on the inner side.

In summary, it is essential to establish the relationship between the macro deformation of a slope and the accumulation of earth pressure in the seismic design of slope engineering. This provides valuable insights into the distribution pattern of earth pressure, thus offering crucial references for the seismic design of slope engineering.

3.3 Cumulative Damage Processes of the Model Slope

Under continuous seismic actions, the slope undergoes cumulative damage, resulting in a progressive failure process. Observations from the series of shaking table tests reveal accumulated damage to the anti-dip bench rock slope due to multiple seismic actions. This damage accumulation includes tension cracking on the inner side of the benches, tension cracking and settlement at the rear edge, and bulging at the slope toe, as shown in Fig. 11. High-speed cameras and digital image correlation were used to record the deformation and crack development processes of the slope. Based on the analysis of recorded images from the high-speed cameras and DIC, the shattering and instability failure process of the anti-dip bench rock slope can be divided into four stages: initial tension crack on the bench inner side, followed by settlement of slope top and bulging at its toe, then overall downwards settlement in slope upper part and shear-sliding in its lower part, and finally, culminating in shattering and collapse of the slope surface induced by strong earthquake.

When the earthquake loading is lower than 0.4 g, the shear effect of the seismic waves on the slope is minimal, and the slope does not exhibit significant deformation. However, data from displacement sensors clearly indicate an increase

in slope displacement response correlating with an increase in the peak ground motion of the earthquake input. This displacement response also shows an upward trend from the slope toe to the slope top, with the deformation being primarily elastic. Once the earthquake loading reaches 0.4 g, the slope toe and the inner side of the second bench start to show tensile cracks. From the side view, the second bench is noticeably wider than the other benches. Therefore, both the slope toe and the inner side of the second bench become areas of stress concentration, leading to the development of tensile cracks under seismic action. As the input seismic amplitude increases, these cracks continue to widen and deepen. Numerous cracks can be seen extending along the weak interlayer, running parallel to each other. These cracks are approximately 10 cm in length and about 1.5 mm in width.

When the earthquake loading reaches 0.6 g, a tensile crack develops along the slope inclination from the slope top, extending to the inner side of the third bench. This crack progresses downward, indicating a tendency to split the slope. Observed from the side view of the slope, these cracks continuously widen and deepen as the input peak ground acceleration increases. The repeated shear effects of seismic waves cause these cracks to open and close cyclically. During the opening phase, small particles fall and accumulate at the crack ends, while during the closing phase, these particles are compressed and moved, creating a wedge-splitting effect that further expands the cracks and progressively destabilizes the slope. Due to the elevation amplification effect, there is a noticeable settlement in the upper part of the slope, with higher elevations experiencing greater settlement. On the outer sides of the benches, where there is less constraint and a larger dynamic response acceleration, the settlement of the outer sides of the second and third benches is more significant than that of the inner sides. As the peak ground acceleration increases, the shear strength of the slope rock mass decreases, leading to the detachment and fall of small rock blocks from the upper part of the slope, which then accumulate on the second bench. These observations indicate that the bench slope surface acts as an environmentally friendly artificial reinforcement method. The presence of multiple benches in the bench slope provides horizontal surfaces that allow the falling rock mass from the upper part of the slope a longer path to disperse and consume energy. This contrasts with a single surface slope where rock blocks could quickly slide to the bottom, releasing a large amount of energy and potentially causing impact forces that could damage important structures, such as buildings and roads in the lower part of the slope, thereby reducing the likelihood of slope failure.

When the earthquake loading reaches 0.9 g, existing cracks not only expand but also deepen, extending downwards and segmenting the slope into blocks that are wider at the top and narrower towards the bottom. Due to stress concentration on the inner sides of the bench, these cracks are particularly pronounced and extend along the strike of the slope. With

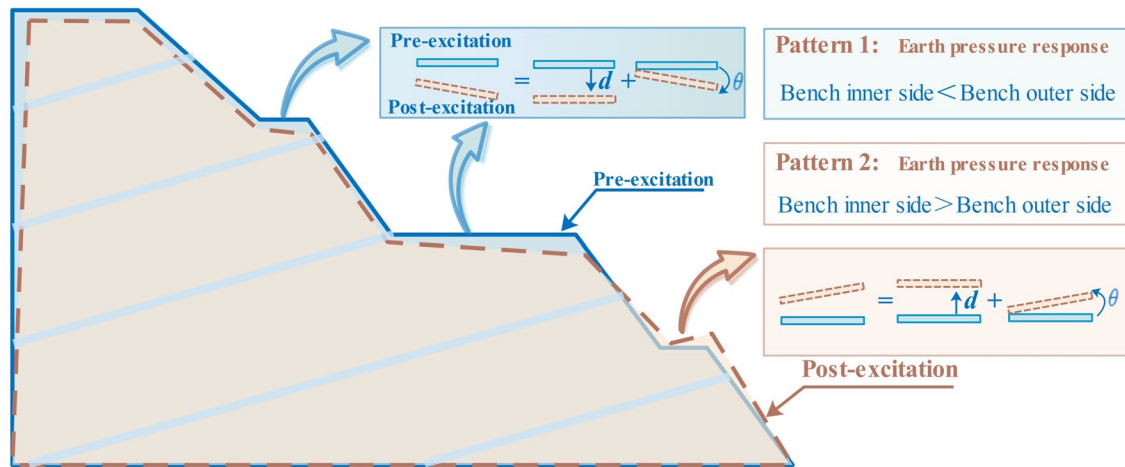


Fig. 10 The macro deformation and earth pressure distribution across each bench of the anti-dip bench rock slope under seismic excitations

ongoing seismic activity, the cracks at the slope top continuously expand and connect with those in the lower part of the slope. This fragmentation reduces the structural integrity of the slope and alters the propagation path of seismic waves, intensifying scattering and reflection phenomena during wave transmission, thereby enhancing the filtering effect of the slope. From a side view, numerous cracks can be seen extending along the direction of the weak interlayer, with the crack propagation exhibiting a tracking effect.

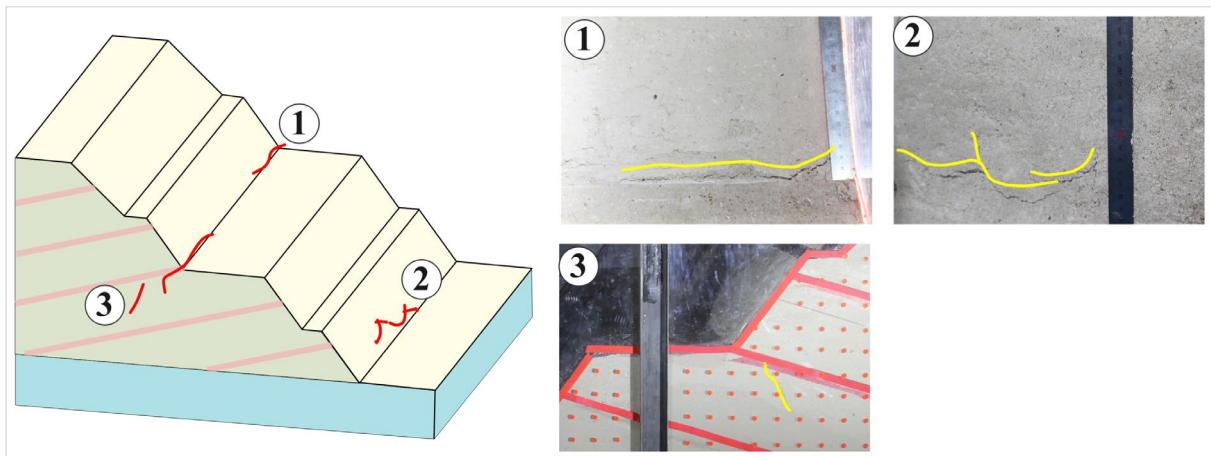
When the earthquake loading reaches 1.3 g, the slope undergoes continuous intense seismic action, resulting in enormous deformation. The rear edge of the slope becomes disengaged from the model container. The second and third benches, as well as the slope top, experience varying degrees of settlement, while a bulge forms at the toe of the slope. A large number of cracks developed across the slope and crisscrossed each other. Multiple cracks can be seen from the side view extending along the slope inclination, indicating shear sliding failure of the slope.

4 Dynamic Numerical Simulation Analysis

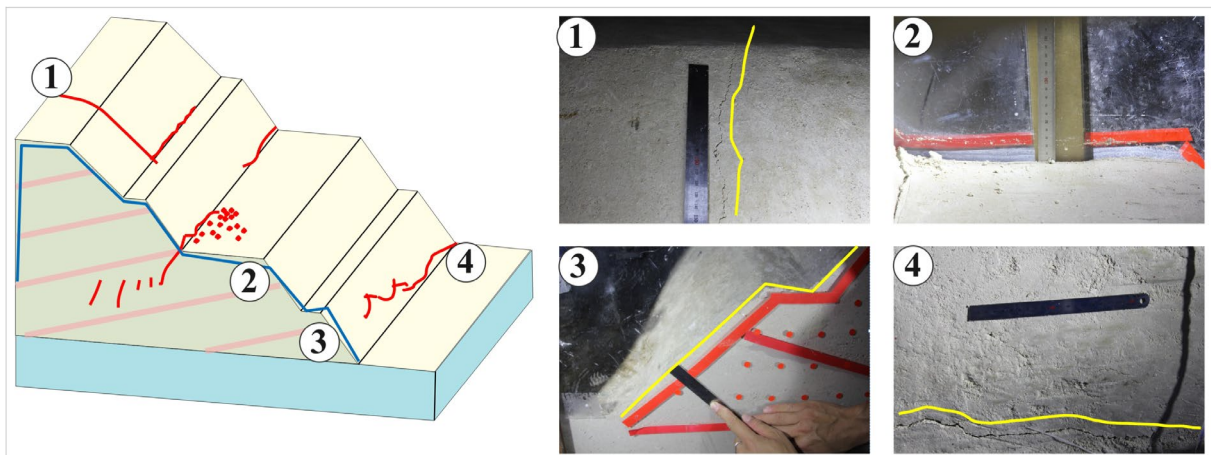
A full-scale anti-dip bench rock slope model was established using the FLAC3D code, as shown in Fig. 12. The original coordinate system was set at the lower left corner of the model. To avoid seismic wave reflections at the boundaries, the left boundary of the model is located 2.5 H away from the rear edge of the slope, and the distance from the slope toe to the right boundary of the model is 1.5 H, where H represents the height of the slope. The total height of the model is 2 H and includes both the rock mass and weak interlayer, with their physical and mechanical parameters detailed in Table 1. In terms of grid division, the maximum size of each grid element is smaller than one-tenth of the highest

frequency component of the input seismic wave. Therefore, in this series of numerical simulation experiments, the maximum grid size was set to 1 m. To compare with the results of the shaking table model tests, the input seismic wave in this series of numerical simulation experiments was identical to the Wenchuan seismic wave used in the shaking table tests. Analyzing the time history curve of the waveform reveals that the Wenchuan seismic wave displays two distinct energy release characteristics and exhibits a pulse-like effect. The acceleration time history was integrated to obtain the velocity time history and displacement time history. It was found that the displacement time history does not return to zero at the endpoint. The Fourier spectrum of the Wolog seismic waves demonstrates the main energy is concentrated within 30 Hz, especially in the range of 0-10 Hz. Additionally, in geotechnical slope engineering, the natural frequencies of slopes are typically low, and excessive excitation frequencies can lead to computational instability in numerical simulations. Therefore, a low-pass filter with a cut-off frequency of 30 Hz was applied to the seismic wave prior to simulation. This filtering prevents a continuous increase in the slope displacement at the end of the seismic excitations and mitigates the impact of high-frequency components on the wave propagation in the numerical model. Additionally, the effect of frequency on the dynamic response of the slope is further analyzed by loading sine waves at different frequencies.

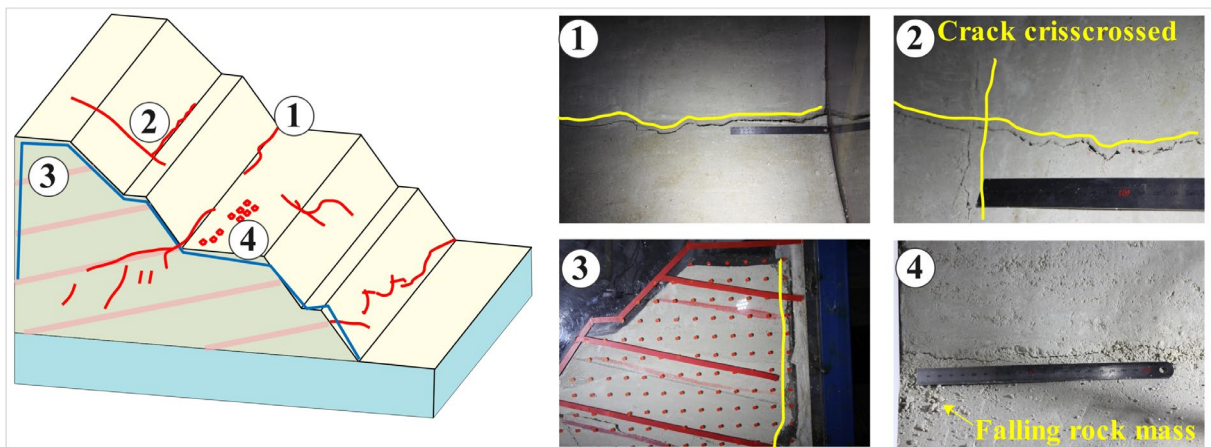
The boundaries of the model play a critical role in the outcomes of numerical simulations. In this series of numerical simulations, free-field boundaries were implemented to prevent seismic wave reflections at the boundaries. These free-field boundaries are treated as infinite field boundaries, effectively reducing or even eliminating the distortion of seismic waves at the edges of the simulation. Damping settings are equally crucial for the reliability of the experimental results. Generally, a common global dissipation model



(a)



(b)



(c)

Fig. 11 The deformation and failure process of the anti-dip bench rock slope. **a** at 0.4 g peak ground acceleration; **b** at 0.6 g peak ground acceleration; **c** at 0.9 g peak ground acceleration; **d** at 1.3 g peak ground acceleration

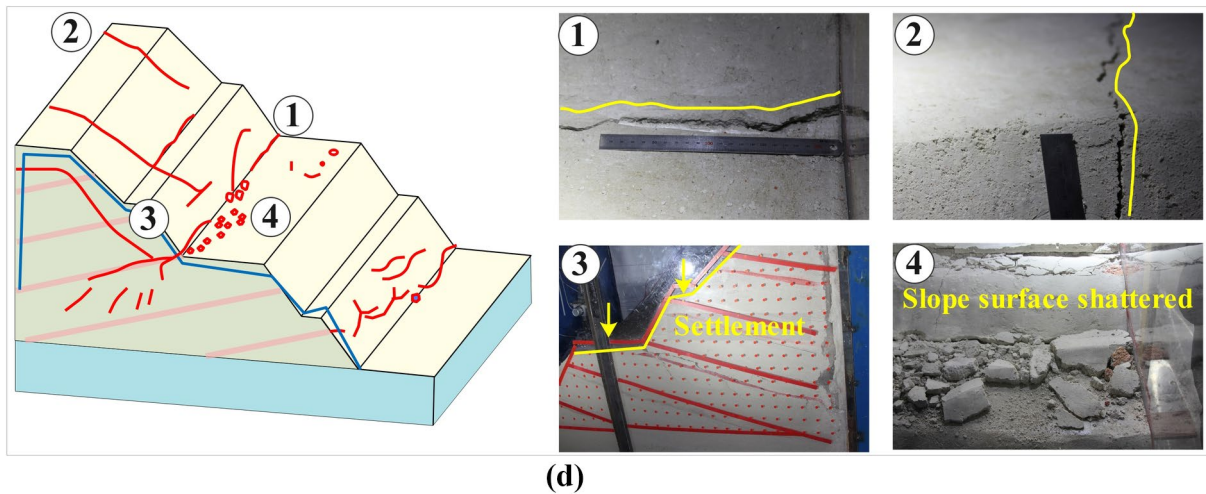


Fig. 11 (continued)

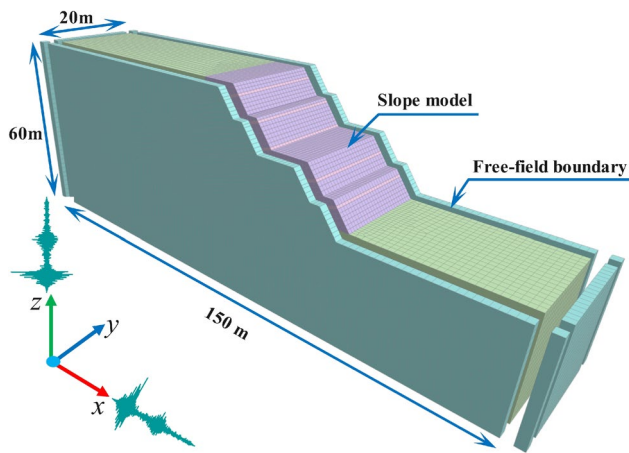


Fig. 12 Numerical simulation model and dynamic boundary setting

is used, introducing additional damping in the numerical simulation to mimic the energy dissipation observed in the rock mass. This is related to the overall stiffness and mass of the slope system and is commonly utilized to characterize the overall damping properties of the materials and the structure itself. Rayleigh damping, often represented in terms of proportional damping or fundamental frequency damping, can be adjusted to match the dynamic characteristics of the system. By setting appropriate Rayleigh damping parameters, the simulation can more accurately model the energy dissipation of the rock mass, enhancing the fidelity of the simulation results. While Rayleigh damping can produce satisfactory experimental results, it necessitates a smaller time step in explicit codes to maintain numerical stability, significantly increasing computation time. In contrast, local damping addresses the limitations of Rayleigh damping by ensuring that the damping force is proportional to the

magnitude of the unbalanced force and always acts opposite to the direction of the current velocity component. This approach enhances computational efficiency. Local damping was set in this series of numerical simulations. The inclusion of local damping can introduce high-frequency noise into the calculation results. Therefore, a low-pass filter was applied to the input seismic wave before starting the numerical simulation to mitigate the impact of high-frequency components on the experimental results. In line with the "Code for Seismic Design of Railway Engineering" (GB 50111–2006), the critical damping ratio is set at 0.05, and the local damping coefficient at 0.157 for these simulations (Verrucci et al. 2022).

Figure 13a–d shows the peak ground displacement response time history of the anti-dip bench rock slope under the 0.6 g Wenchuan wave, with inputs in both horizontal and vertical directions. From the displacement time history, it can be observed that there are displacement baseline offsets at various locations on the slope under seismic action, indicative of residual deformation in the slope. For the first, second, and third benches, the peak ground displacement response on the outer side of each bench is greater than that on the inner side. This discrepancy occurs because the outer sides of the benches, being the bulging parts of the slope, are less constrained and have greater freedom of movement than the inner sides. Moreover, the mechanical parameters on the bench outer side deteriorate continuously under multiple seismic actions, accumulating plastic deformation and leading to a more pronounced peak ground displacement response compared to the bench inner sides. It is particularly noteworthy that the peak ground displacement response on the inner side of the second bench is the smallest among the three benches. This indicates that a wide bench can effectively mitigate the displacement response of the slope. Such

a configuration can transform the overall failure of the slope into localized failure, thereby reducing the peak ground displacement response of the entire slope.

By comparing the results of shaking table tests with numerical simulations, the accuracy and reliability of the numerical model can be validated. The peak ground displacement data from both methods were analyzed under varying input peak ground accelerations, focusing on four distinct monitoring points on the slope surface: D1, D3, D5, and D7. The first three points are located on the outer side of the bench, while the fourth point is located at the slope top. Since the geometric dimensions of the numerical model are identical to those of the prototype, the displacements obtained from the shaking table tests were scaled by the geometric similarity ratio before comparison with the numerical simulation results.

As shown in Fig. 13e–h, under low-amplitude seismic loading (0.1g to 0.4g), the results from the shaking table tests and numerical simulations exhibit a high degree of agreement. This consistency indicates that before the slope transitions into a plastic state, the numerical simulation can accurately capture the dynamic response of the slope under seismic excitation. Within this loading range, the peak displacements from the model tests closely align with those from the numerical simulations, confirming the validity and reliability of the numerical model for analyzing slope dynamic responses.

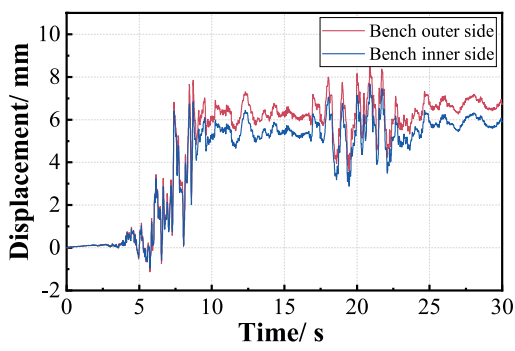
However, as the amplitude of the input seismic waves increases from 0.6 to 1.0 g, discrepancies emerge between the shaking table tests and numerical simulations. These differences become particularly pronounced when the input peak acceleration exceeds 0.6g. This divergence is primarily attributed to the substantial nonlinear behavior exhibited by the rock materials once the slope enters a plastic state. In this state, the deformation and failure mechanisms of the slope become significantly more complex, leading to deviations between numerical simulation predictions and the actual test observations.

Figure 14a–d show the displacement dynamic response contour map under the loading of 3 Hz, 5 Hz, 7 Hz, and 10 Hz sine waves with an input peak ground acceleration of 0.6 g. Figure 14e represents the displacement dynamic response under the action of the Wenchuan earthquake with the same input acceleration, while Fig. 14f illustrates the final failure state of the slope under the Wenchuan earthquake motion during the shaking table test. From Fig. 14a–d, it is evident that as the input frequency increases, the displacement response of the slope transitions from overall to localized deformation. Specifically, the low-frequency components of the seismic waves induce overall deformation of the slope, whereas the high-frequency components lead to localized deformation. High-frequency components, with their shorter periods, cause relative displacements between particles as

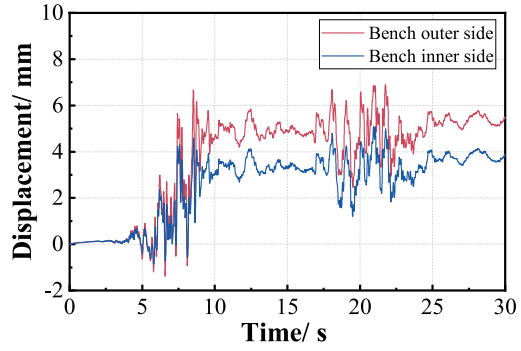
they propagate through the slope. This activity promotes the formation of micro-cracks on the slope surface or at the contact points of different lithologies, leading to particle rearrangement and local shear sliding, which in turn results in localized deformation. Conversely, the low-frequency components, with their longer periods, allow more time for the rock mass to react to seismic forces. This extended interaction period enables horizontal sliding and tilting within the slope, contributing to its overall deformation. It is worth noting that when a 3 Hz sine wave is applied, its frequency closely aligns with that of the Wenchuan earthquake, leading to a more uniform distribution of peak ground displacement responses throughout the slope. The displacement contour map indicates that a wide platform can transform the overall failure of the slope into localized failure, making it more favorable for seismic resistance in slope engineering. Figure 14e and f depict the final failure state of the anti-dip bench rock slope under the action of the Wenchuan earthquake in both numerical simulations and shaking table tests, revealing consistent deformation states. The top, second, and third benches of the slope show varying degrees of settlement deformation, while the first bench exhibits some bulging.

Figure 15 shows the time history curves of shear strain increments at various locations on the slope surface. In the dynamic response analysis of rock slopes, these shear strain increments represent the increase in strain caused by shear deformation of the rock mass under seismic excitations. They reflect the relative increment of shear displacement at different positions within the rock mass compared to the initial state and can be used to identify potential sliding surfaces, cracks, and other sensitive areas within the rock mass. Analyzing the shear strain increments of the slope under seismic excitations allows for a detailed study of the deformation and failure characteristics of the slope. This analysis is instrumental in assessing the safety and stability of the slope and provides valuable insights for seismic design and reinforcement strategies. When the shear strain increment is positive, it indicates a degree of positive shear deformation within the rock mass, suggesting relative sliding or shearing between particles. Positive shear strain increments typically correspond to phenomena such as extension or opening in the direction of the vertical propagation of seismic waves. Conversely, negative shear strain increments indicate a degree of reverse shear deformation in the rock mass, signifying relative compression or closure between particles. These insights are essential for understanding the dynamic responses of slopes to seismic forces and tailoring appropriate engineering responses.

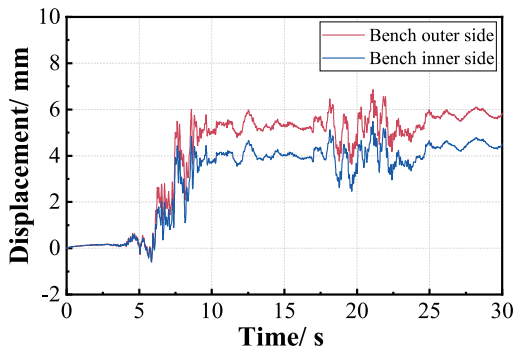
In this series of numerical simulations on anti-dip bench rock slopes, the time history of shear strain increments at different locations on the slope surface reveals that the inner



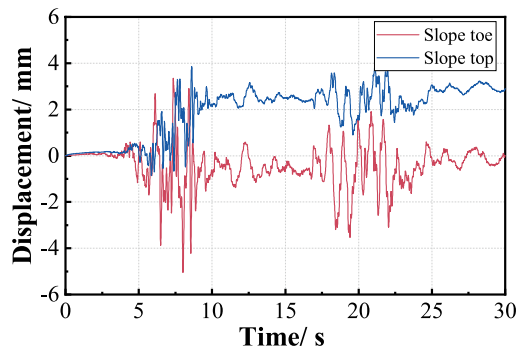
(a)



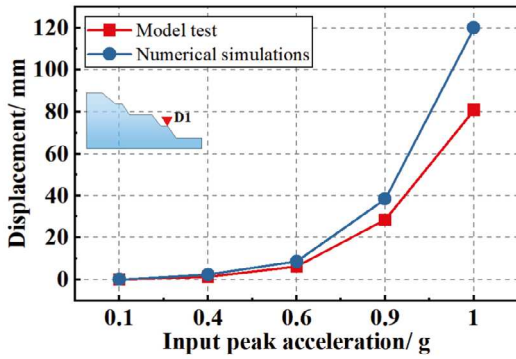
(b)



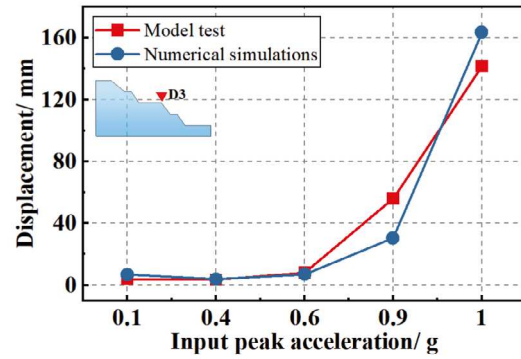
(c)



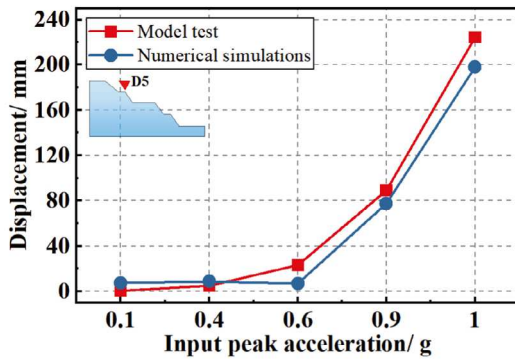
(d)



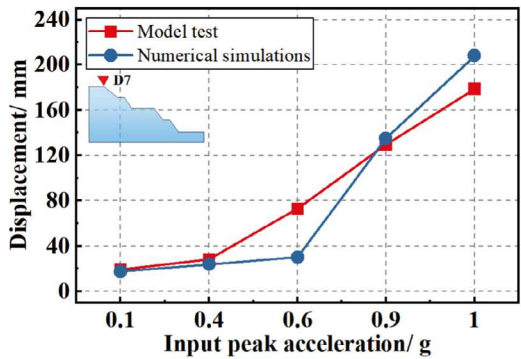
(e)



(f)



(g)



(h)

Fig. 13 The peak ground displacement response time history curves of the anti-dip bench rock slope to a 0.6 g Wenchuan wave excitation and Comparison of experimental results between numerical simulation and shaking table tests. **a** the peak ground displacement response of the first bench; **b** the peak ground displacement response of the second bench; **c** the peak ground displacement response of the third bench; **d** the peak ground displacement response of the slope toe and slope top; **e** D1 monitoring point; **f** D3 monitoring point; **g** D5 monitoring point; **h** D7 monitoring point

side of the first bench and the slope toe exhibit the largest shear strain increments. This observation indicates that these areas are particularly susceptible to deformation and cracking under seismic action, aligning with seismic failure patterns noted in the shaking table tests. Specifically, the first bench shows a negative shear strain increment on the inner side (indicating compression) and a positive increment on the outer side (indicating tension), corroborating the results from the earth pressure analysis. The deformation of the bench includes both translational and rotational displacements. For the third and second benches, the outer side rotates around the inner side, resulting in greater compression and consequently, a higher earth pressure response on the outer side. However, the first bench exhibits an opposite pattern of earth pressure distribution, where the inner side experiences compression and the outer side tension. Figure 16a depict the shear strain increment contour plots under the loading of the Wenchuan earthquake wave and the failure state of the second bench inner side. Figure 16b depict the shear strain increment contour plots under the loading of the 3 Hz sine wave and the failure state of the bench toe. The contour maps reveal that the inner side of the second bench and the slope toe exhibit the highest shear strain increments, indicating these areas are the most susceptible to cracking. Additionally, a wide bench is shown to transform overall deformation into localized deformation, enhancing seismic resistance. This design strategy, employing both wide and narrow platforms on the bench slope, proves beneficial for the structural stability of slope engineering.

5 Discussion

5.1 Cyclic Tension–Compression Cycles and Tensile-Shear Fracturing in Rock Masses

The stress state and stress levels within a rock mass significantly influence the failure mechanics of slopes. In engineering contexts, rock masses are typically subjected to compressive stress, with shear failure being the predominant failure mode for both rocks and soil. Earthquakes can cause instantaneous changes in the stress field of slopes, leading to alternating positive and negative changes in the magnitude and direction of stress within the elements. This phenomenon

primarily manifests as the instantaneous alternation between compressive and shear stress states.

Assuming that the elements within the slope can be analyzed as a plane strain problem, an element can be extracted from the slope for detailed analysis. When the slope is in a static state, the maximum and minimum principal stresses are represented by Formulas (9) and (10), respectively (Fang et al. 2024).

$$\sigma_1 = \frac{\sigma_x + \sigma_z}{2} + \sqrt{\left(\frac{\sigma_x - \sigma_z}{2}\right)^2 + \tau_{xz}^2} \quad (9)$$

$$\sigma_3 = \frac{\sigma_x + \sigma_z}{2} - \sqrt{\left(\frac{\sigma_x - \sigma_z}{2}\right)^2 + \tau_{xz}^2} \quad (10)$$

where σ_x , σ_z represent the horizontal and vertical stresses, respectively, and, τ_{xz} is the shear stress.

When the slope is subjected to horizontal seismic excitation, it induces additional shear stress τ_s in the stress state of the element. The magnitude and direction of τ_s are influenced by the input seismic waves, and the stress state can be represented by Formulas (11) and (12) (Li et al. 2024).

$$\sigma'_1 = \frac{\sigma_x + \sigma_z}{2} + \sqrt{\left(\frac{\sigma_x - \sigma_z}{2}\right)^2 + (\tau_{xz} + \tau_s)^2} \quad (11)$$

$$\sigma'_3 = \frac{\sigma_x + \sigma_z}{2} - \sqrt{\left(\frac{\sigma_x - \sigma_z}{2}\right)^2 + (\tau_{xz} + \tau_s)^2} \quad (12)$$

The formula for calculating τ_s is as follows: $\tau_s = \rho C_s v_s$, where ρ is the mass density, C_s is the velocity of s wave propagating in rock mass, and v_s is the input shear velocity induced by seismic excitation in the horizontal direction.

Under the action of earthquakes, the stress state of rock masses is a combination of static stress and additional dynamic stress induced by seismic loading. As the magnitude and direction of dynamic stress constantly changing, the seismic excitation modifies the original stress state of the slope, leading to deformation and eventually causing instability. The Mohr's stress circle in initial stress state and stress state under seismic load is shown in Fig. 17a.

In the Mohr's stress circle, seismic excitation causes variations in the difference between the maximum and minimum principal stresses. As a result, the radius of the Mohr's stress circle fluctuates, either increasing or decreasing, while its center continuously moves along the stress axis. These changes in the stress state of the element can lead to three possible conditions relative to the Mohr's stress and the shear strength: no shear failure, incipient shear failure, and shear failure. When the minimum principal stress σ'_3 is less than zero and greater than the dynamic tensile strength of the rock, the element experiences tensile failure. Considering the relationship between the Mohr's stress circle and

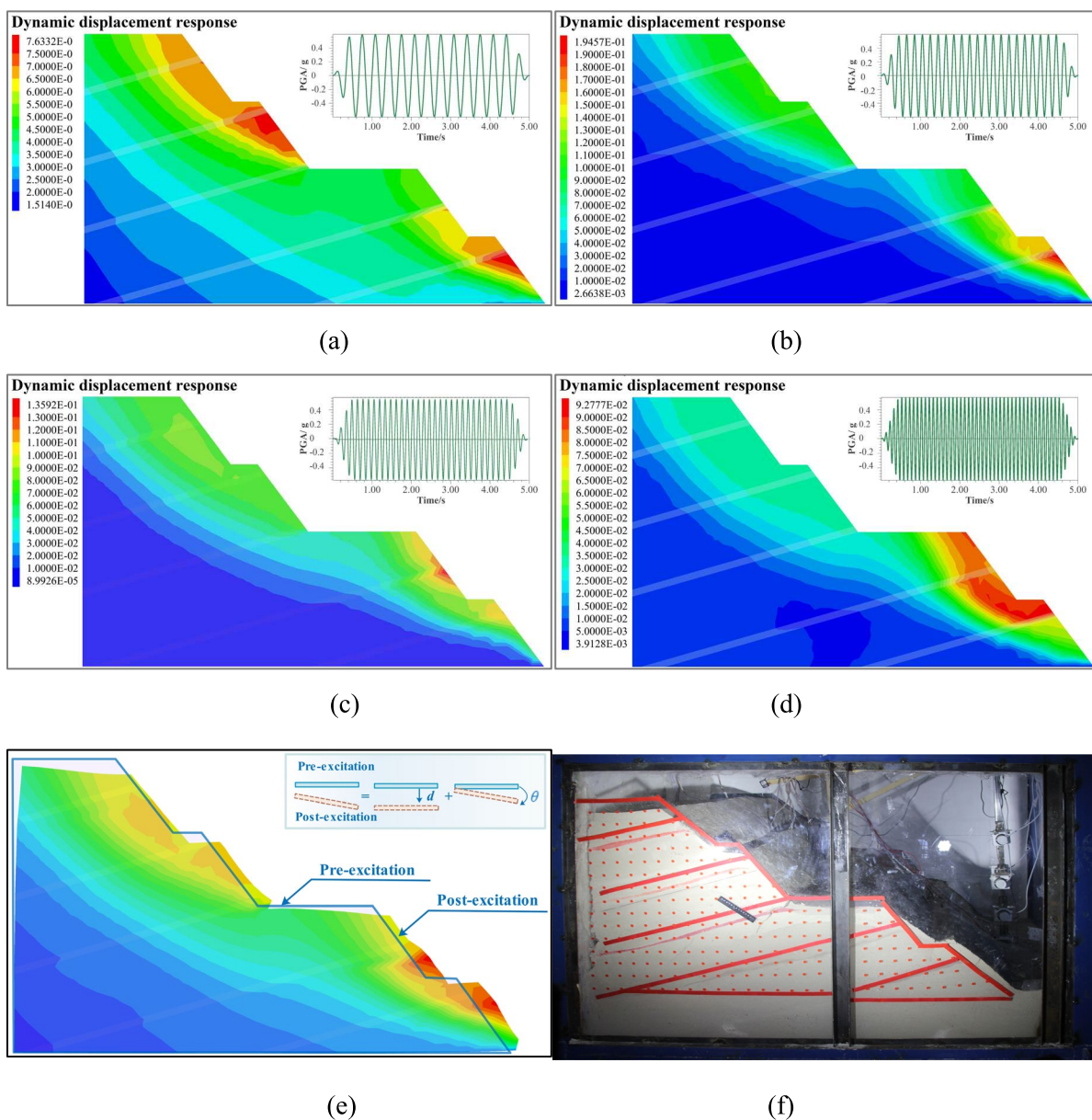


Fig. 14 The displacement dynamic response contour map and final failure state of the anti-dip bench rock slope. **a** excited by a 3 Hz sine wave; **b** excited by a 5 Hz sine wave; **c** excited by a 7 Hz sine wave;

d excited by a 10 Hz sine wave; **e** excited by a Wenchuan wave; **f** the final failure state of the anti-dip bench rock slope

the envelope of shear strength, there are four distinct stress state conditions for rock masses under seismic excitations, as shown in Fig. 17b. Case 1: The rock element is in a compressive-shear state under seismic excitation. Both σ_1 and σ_3 are increased compared to the natural state. Case 2: The rock element undergoes a tensile-shear state, where σ_1 increases but σ_3 decreases to less than zero compared to the natural state. Case 3: The rock element is in a compressive-shear state, which σ_1 decreases and σ_3 increases compared to the natural state. Case 4: The rock element exhibits a tensile-shear state, characterized by a decrease in both σ_1 and σ_3

compared to the natural state, with σ_3 dropping below zero in this instance.

The stress trajectories within the slope and the possible failure mode of the slope are illustrated in Fig. 17c. Based on the stress state of the unit body, the analyzed failure modes include tension failure, tension-shear failure, shear failure, and compression-shear failure. Tension failure usually occurs at the top or edge of the slope, especially under the action of earthquakes or other external forces. In these areas, tensile forces acting on the rock induce crack formation and propagation. Tension-shear failure usually is

Fig. 15 The shear strain increment time history curves of the anti-dip bench rock slope under a 0.6 g Wenchuan wave excitation. **a** the shear strain increments of the first bench; **b** the shear strain increments of the second bench; **c** the shear strain increments of the third bench; **d** the shear strain increments of the slope toe and slope top

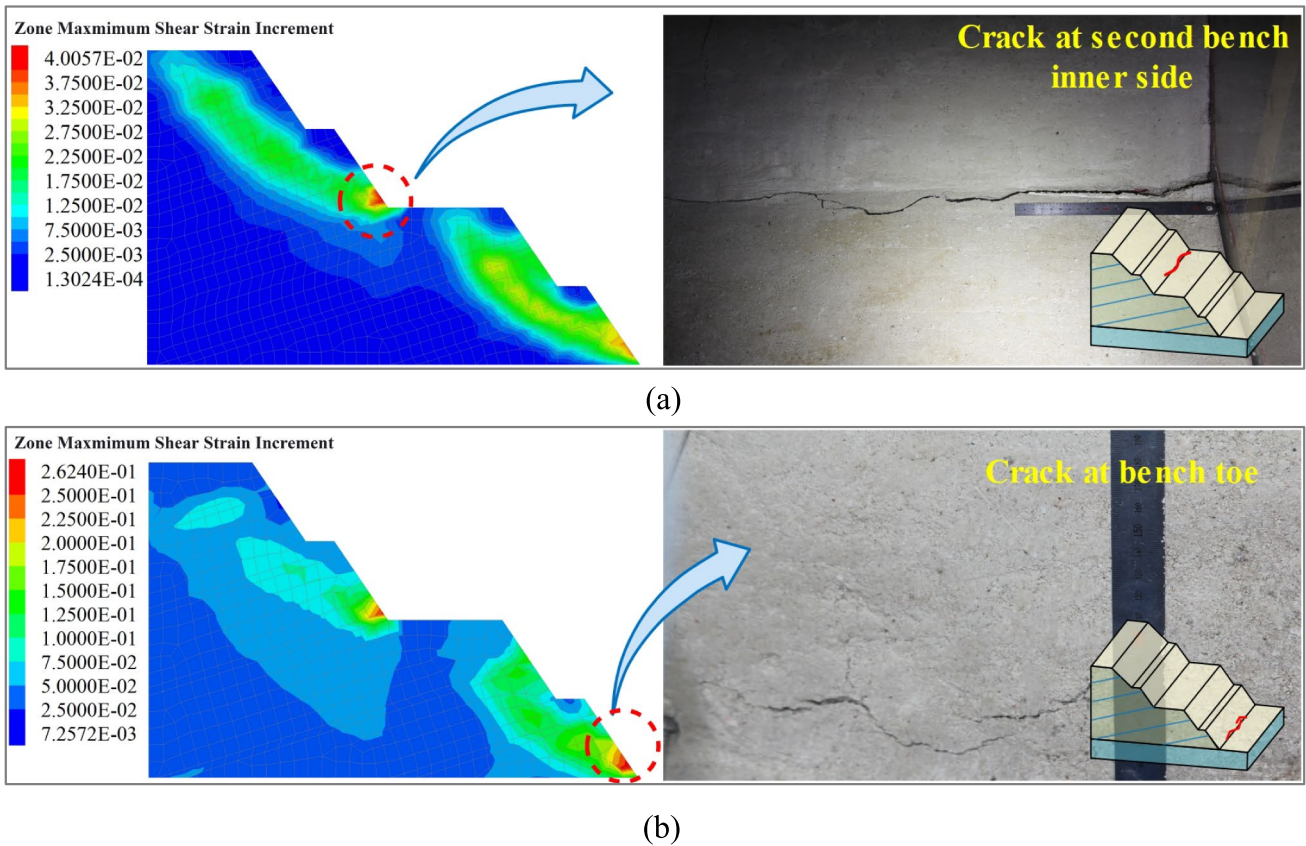
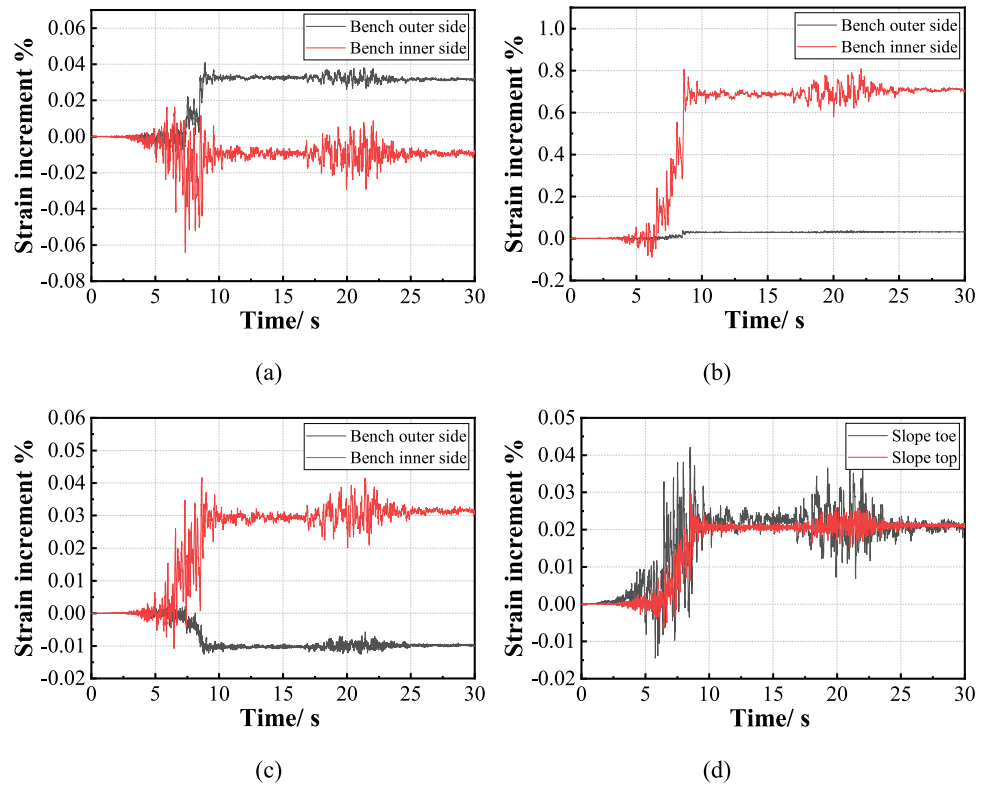
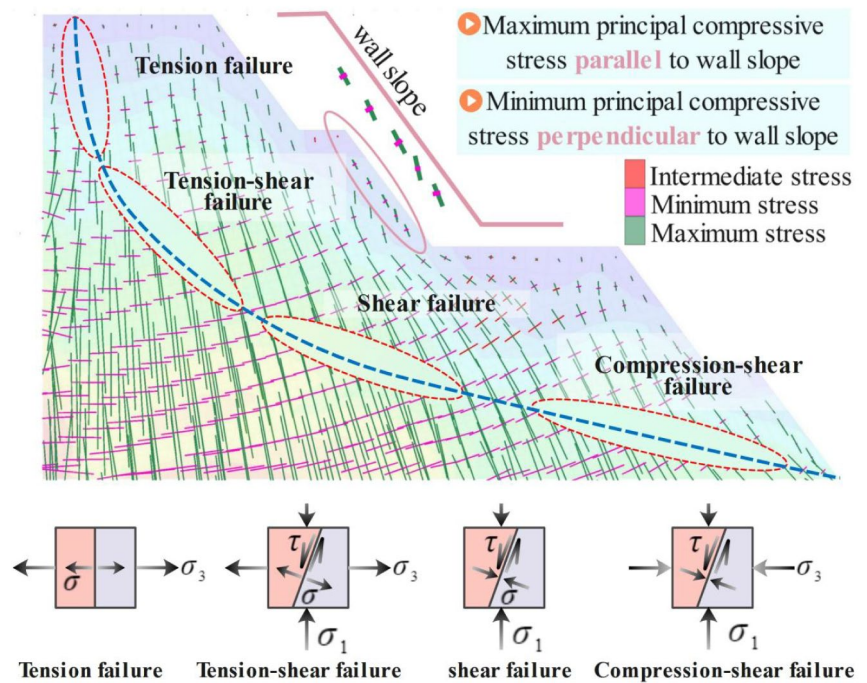
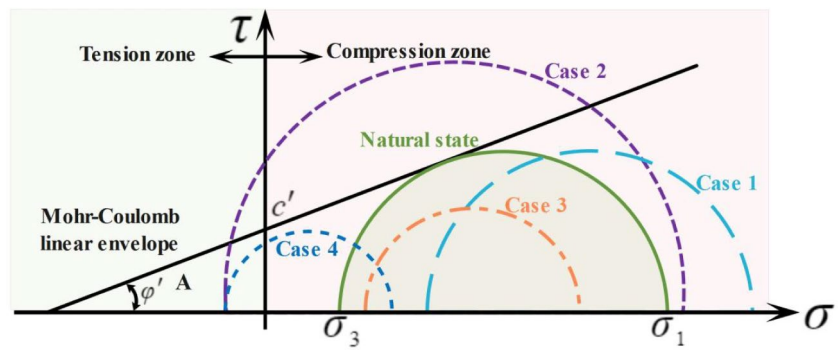
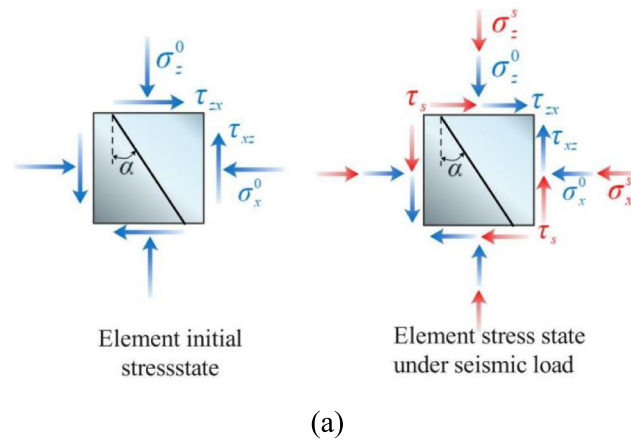


Fig. 16 The shear strain increment contour plots and failure state of the anti-dip bench rock slope. **a** excited by Wolong seismic wave and the failure state of the second bench inner side; **b** excited by a 3 Hz sine wave and the failure state of the bench toe

Fig. 17 The stress state and the failure pattern of the rock slope. **a** stress state of the rock under earthquake excitation; **b** the Mohr's stress circle and the envelope of shear strength; **c** the stress trajectories within the slope and the possible failure mode of the slope; **d** the tension cracks at the slope top of Shiziliang; **e** the tension cracks at the slope top in the shaking table test; **f** the bulging cracks at the slope toe of Shigongping landslides in Qingchuan; **g** the bulging cracks at the slope toe in the shaking table test



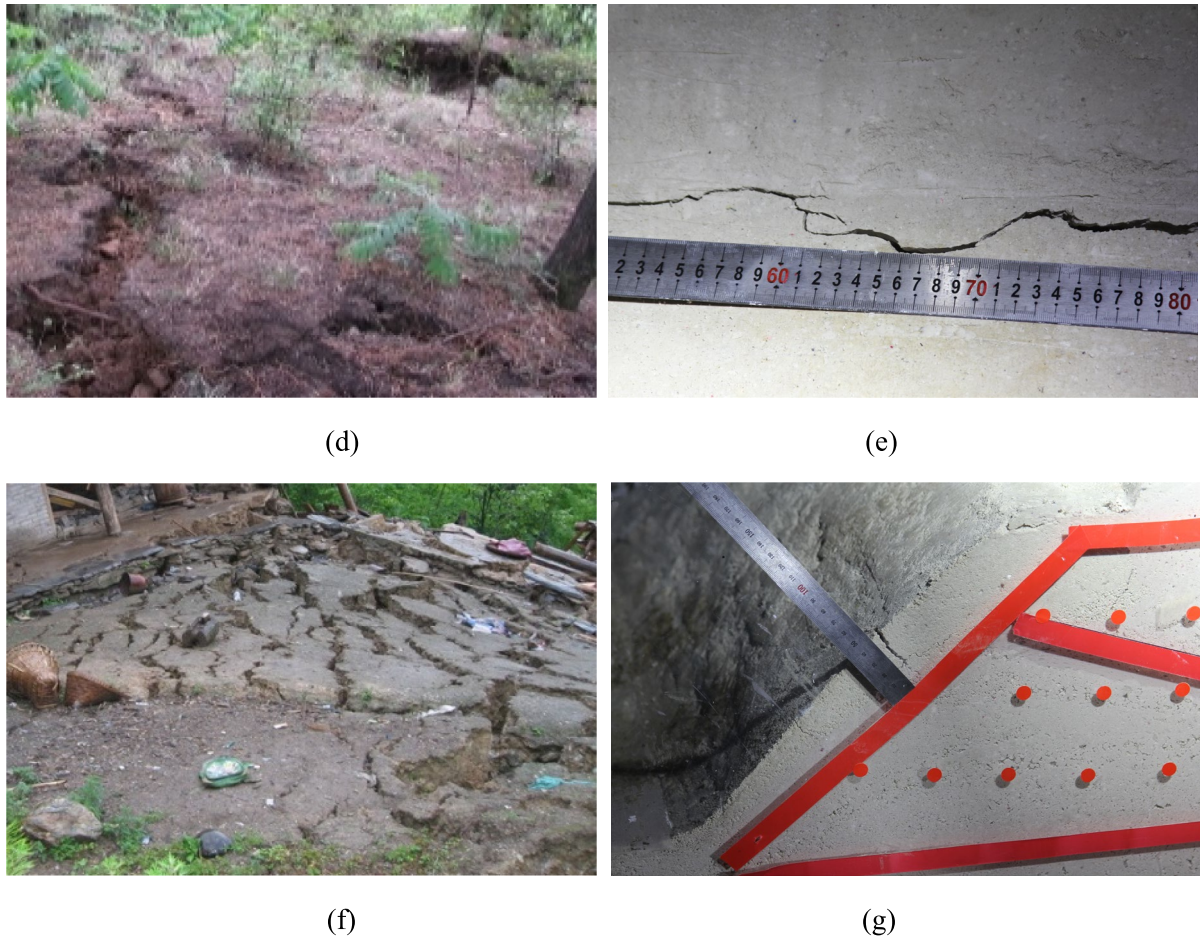


Fig. 17 (continued)

commonly observed in the middle and upper parts of the slope when subjected to the combined tensile and shear forces. This type of failure often results in localized instability and the development of sliding surfaces. Shear failure is prevalent in the middle and lower parts of the slope, primarily due to horizontal shear forces. Such failures frequently lead to slope sliding and the creation of sliding surfaces. Compression-shear failure is typically found in the lower part of the slope, occurring under the combined effects of vertical pressure and horizontal shear forces. This mode of failure often causes deep-seated sliding and the formation of larger sliding surfaces.

Under the action of strong seismic horizontal inertial forces, a tensile crack typically first emerges at the rear edge of the slope. With the continuous excitations during the earthquake, both tensile cracking and shear sliding deformation evolve at the bottom of the crack, eventually forming a sliding surface that leads to slope instability along this plane. The Wenchuan earthquake triggered a large number of slope failures that exhibited this cracking-shear-sliding pattern, including notable events such as the Wangjiayan landslide in Beichuan, the Guershan landslide in Chenjiaba

of Beichuan, the Dongjia landslide in Qingchuan, and the Guantan landslide in Anxian (presented by Fig. 17d and f). The same pattern, including tension cracks at the slope top and bulging at the toe, was also replicated in shaking table tests (see Fig. 17e and g). Therefore, the cracking-shear-sliding mechanism is recognized as the fundamental geological-mechanical pattern contributing to large-scale landslide failures under intense seismic forces.

5.2 Wedge Splitting Effects and Crack Propagation in Rock Masses

The seismic wave body wave includes both P wave and S wave. The vertical vibrations caused by P-waves and the horizontal vibrations induced by S-waves can lead to changes in the movement trends of rock masses, often in opposing directions. The interplay between these two wave types will determine the movement trends of the slope and its potential failure mode. The displacement vector diagrams of the slope under the excitation of the Wenchuan seismic wave at different times are shown in Fig. 18a and b. In general, the vertical acceleration produced by the P wave is less than the gravitational acceleration. The

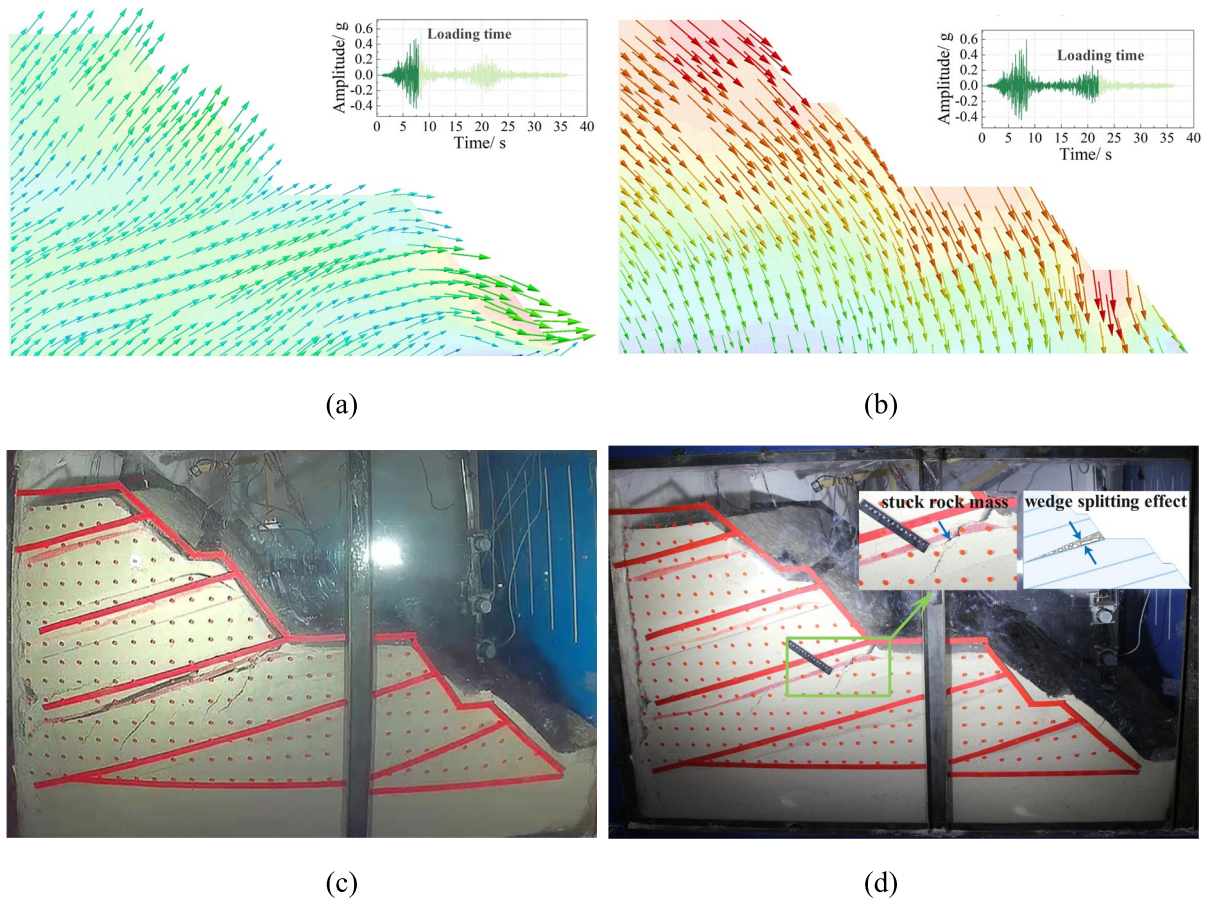


Fig. 18 The displacement vector diagram of the slope under Wenchuan seismic wave excitation at different times. **a** at 8 s; **b** at 23 s; **c** rock mass separation; **d** wedge splitting effect

inertia force generated by the P wave can cause the gravitational field of the slope to experience either overloading or unloading, thus increasing or decreasing the slope gravitational deformation tendency. When the slope is subjected to the combined effects of P waves and S waves, the resultant inertia force direction is toward the upper right, which may cause the slope to exhibit ejection-like tendencies. As stress wave traverses through weak interlayers, the contrasting properties of the media on either side create reflected waves. This results in both reflected wave stress and transmitted wave stress at the interface. Near the weak interlayer, there is a dynamic stress differentiation due to the reflection mechanism of stress waves. Specifically, when a stress wave transitions from the rock mass to a weak interlayer with a lower elastic modulus, the reflected wave becomes a tensile wave, producing tensile stress at the interface between the rock mass and the interlayer. In addition, the greater the difference in the elastic modulus of the rock mass near the interface, the more pronounced the

tensile stress, negatively impacting the stability of the rock mass. Cracks that exhibit opening and filling behavior, indicative of medium changes, also generate reflected wave stress and promote further opening and cracking. In the series of shaking table tests, video footage from high-speed cameras shows that under the action of seismic waves, the slope experiences tensile stress at the weak interlayer, resulting in the separation of the rock mass, as shown in Fig. 18c. The repeated tensile shear action of seismic waves creates surface cracks on the slope, allowing rocks to fall inward upon crack opening. These fallen rock blocks exert a wedge effect during counter-compression of the slope, further widening and extending the cracks. Due to the periodic nature of seismic inertia forces, the vertical plane can form an opening displacement during the tension half cycle with fine particles on the top filling it under gravity. In the compression half cycle, these filling materials are compacted, leaving a small opening displacement since the openings cannot completely close. Under repeated vertical openings, new openings continuously form, and particles fall and fill these gaps, becoming compacted during reciprocating compression.

This ongoing process leads to the continuous generation of new residual tension displacement, as shown in Fig. 18d.

6 Conclusions

This study employed large-scale shaking table tests and numerical simulations to investigate the deformation and failure mechanisms of anti-dip bench rock slopes under seismic excitations. The introduction of the displacement baseline offset ratio provided a novel approach to quantify the instability and failure process of slopes after reaching the plastic state. The findings of this study offer theoretical insights into the deformation and failure mechanisms of anti-dip bench rock slopes under seismic excitations, contributing to the risk assessment and seismic design of such slopes in earthquake-prone regions. The key findings and conclusions are summarized as follows:

1. Seismic excitations trigger a pronounced displacement amplification effect at elevated parts of the slope. As the input frequency of the sine wave increases, the displacement response in the upper regions of the slope becomes more pronounced.
2. Among all the benches, the second bench is the widest, effectively dividing the slope into two distinct segments. This division not only impedes the deformation and failure processes within the slope but also diminishes the stress conveyed from the upper slope, thus preventing stress concentration at the slope toe and mitigating negative impacts on the upper regions.
3. The DBOR distribution revealed that plastic deformation was more pronounced on the inner sides of benches compared to the outer sides, indicating the inner sides as the initial zones to manifest cracking under seismic excitations.
4. Displacement mutation serves as a criterion for identifying potential instability and the likelihood of failure within slopes. Critical displacement thresholds for seismic damage on each bench have been established by analyzing the residual displacement responses on the inner side of each bench of the anti-dip bench rock slope, coupled with the critical acceleration peak that induces a sharp increase in residual displacement. These thresholds align with the California Geological Survey's benchmarks for shallow slope failure, which range from 0 to 150 mm.
5. Low-frequency seismic wave components are responsible for the overall deformation of the slope, whereas high-frequency components contribute to localized deformation. As localized deformations accumulate to a critical extent, they precipitate a comprehensive sliding failure of the slope.
6. The cyclic tension–compression cycles induced by seismic waves led to tensile-shear fracturing in the rock mass. A cracking-shear-sliding mechanism was identified

as the fundamental geological-mechanical pattern contributing to large-scale landslide failures under intense seismic forces.

7. The wedge-splitting effect, caused by the opening and closing of cracks during seismic excitations, facilitated the propagation of cracks within the rock mass, progressively destabilizing the slope.
8. The dynamic earth pressure response exhibited a resonance phenomenon, with the maximum dynamic earth pressure occurring at an input frequency of approximately 15 Hz. The earth pressure on each bench in the lower part was higher than on the upper part.

Acknowledgements This research was supported by the National Natural Science Foundation of China (Grant No. 52108361 and 41977252), the Sichuan Science and Technology Program of China (Grant No.2024ZYD0154, 2023YFS0436 and 2024NSFSC0159), and the State Key Laboratory of Geohazard Prevention and Geoenvironment Protection Independent Research Project (Grant No. SKLGP2022Z015 and SKLGP2020Z001). All authors acknowledge the anonymous reviewers for their comments.

Funding This research was supported by the National Natural Science Foundation of China (Grant No. 52108361 and 41977252), the Sichuan Science and Technology Program of China (Grant No.2024ZYD0154 and 2024NSFSC0159), and the State Key Laboratory of Geohazard Prevention and Geoenvironment Protection Independent Research Project (Grant No. SKLGP2022Z015 and SKLGP2020Z001). All authors acknowledge the anonymous reviewers for their comments.

Data Availability The original data supporting the conclusions of this article will be made available by the authors, without undue reservation.

Declarations

Conflict of interest The authors declare that they have no known competing financial interests or personal relationships that could have appeared to influence the work reported in this paper.

Open Access This article is licensed under a Creative Commons Attribution 4.0 International License, which permits use, sharing, adaptation, distribution and reproduction in any medium or format, as long as you give appropriate credit to the original author(s) and the source, provide a link to the Creative Commons licence, and indicate if changes were made. The images or other third party material in this article are included in the article's Creative Commons licence, unless indicated otherwise in a credit line to the material. If material is not included in the article's Creative Commons licence and your intended use is not permitted by statutory regulation or exceeds the permitted use, you will need to obtain permission directly from the copyright holder. To view a copy of this licence, visit <http://creativecommons.org/licenses/by/4.0/>.

References

- Bao N, Chen JF, Sun R, Yan KM, Shi ZM (2024) Seismic response of soil arching in pile-reinforced soil slopes: insights from shaking table tests. *Soil Dyn Earthq Eng* 184:108852. <https://doi.org/10.1016/j.soildyn.2024.108852>

- California Geological Survey (2008) Guidelines for evaluating and mitigating seismic hazards in California [M]. California Geological Survey Publication, California, pp 1–40
- Cao LC, Zhang JJ, Wang ZJ, Liu FC, Liu Y, Yang YY (2019) Dynamic response and dynamic failure mode of the slope subjected to earthquake and rainfall. *Landslides*. <https://doi.org/10.1007/s10346-019-01179-7>
- Che AL, Yang HK, Wang B, Ge XR (2016) Wave propagations through jointed rock masses and their effects on the stability of slopes. *Eng Geol* 2016(201):45–56. <https://doi.org/10.1016/j.enggeo.2015.12.018>
- Chen CC, Li HH, Chiu YC, Tasi YK (2020a) Dynamic response of a physical anti-dip rock slope model revealed by shaking table tests. *Eng Geol*. <https://doi.org/10.1016/j.enggeo.2020.105772>
- Chen GP, Yang CW, Tong XH, Wen H, Yue M (2023) Shaking table test on dynamic response of a deposit slope with a weak inter-layer reinforced by the pile-anchor structure. *Soil Dyn Earthq Eng* 170:107912. <https://doi.org/10.1016/j.soildyn.2023.107912>
- Chen JC, Wang LM, Pu XW, Li FX, Li TL (2020b) Experimental study on the dynamic characteristics of low-angle loess slope under the influence of long-and short-term effects of rainfall before earthquake. *Eng Geol* 273:105684. <https://doi.org/10.1016/j.enggeo.2020.105684>
- Dang WG, Tao K, Chen XF (2022) Frictional behavior of planar and rough granite fractures subjected to normal load oscillations of different amplitudes[J]. *J Rock Mech Geotech Eng* 14(3):746–756. <https://doi.org/10.1016/j.jrmge.2021.09.011>
- Dong S, Feng WK, Yin YB, Hu W, Dai HC, Zhang GQ (2020) Calculating the permanent displacement of a rock slope based on the shear characteristics of a structural plane under cyclic loading. *Rock Mech Rock Eng* 53:4583–4598. <https://doi.org/10.1007/s00603-020-02188-y>
- Dong JY, Wang C, Huang ZQ, Yang JH, Xue L (2022) Shaking table model test to determine dynamic response characteristics and failure modes of steep bedding rock slope. *Rock Mech Rock Eng* 55(6):3645–3658. <https://doi.org/10.1007/s00603-022-02822-x>
- Dong JY, Wang C, Huang Z, Yang J, Xue L (2021) Dynamic response characteristics and instability criteria of a slope with a middle locked segment. *Soil Dyn Earthq Eng*. <https://doi.org/10.1016/j.soildyn.2021.106899>
- Fan G, Zhang JJ, Wu JB, Yan KM (2016) Dynamic response and dynamic failure mode of a weak intercalated rock slope using a shaking table. *Rock Mech Rock Eng* 49(8):3243–3256. <https://doi.org/10.1007/s00603-016-0971-7>
- Fan G, Zhang LM, Zhang JJ, Ouyang F (2017) Energy-based analysis of mechanisms of earthquake-induced landslide using hilbert-huang transform and marginal spectrum. *Rock Mech Rock Eng* 50(9):2425–2441. <https://doi.org/10.1007/s00603-017-1245-8>
- Fan G, Zhang LM, Zhang JJ, Yang CW (2019) Analysis of seismic stability of an obsequent rock slope using time-frequency method. *Rock Mech Rock Eng* 52(10):3809–3823. <https://doi.org/10.1007/s00603-019-01821-9>
- Fang K, Fu Y, Tang H, Gao T, An P, Wu Q (2024) Landslide model tests with a miniature 2D principal stress sensor. *J Rock Mech Geotech Eng*. <https://doi.org/10.1016/j.jrmge.2023.12.025>
- He K, Li YJ, Ma GT, Hu XW, Liu B, Ma ZG, Xu ZP (2020) Failure mode analysis of post-seismic rockfall in shattered mountains exemplified by detailed investigation and numerical modelling. *Landslides* 18(1):425–446. <https://doi.org/10.1007/s10346-020-01532-1>
- He JX, Qi SW, Zhan ZF, Guo SF, Li CL, Zheng BW, Huang XL, Zou Y, Yang GX, Liang N (2021) Seismic response characteristics and deformation evolution of the bedding rock slope using a large-scale shaking table. *Landslides* 18(8):2835–2853. <https://doi.org/10.1007/s10346-021-01682-w>
- Li HB, Li XW, Ning Y, Jiang SF, Zhou JW (2019) Dynamical process of the Hongshiyuan landslide induced by the 2014 Ludian earthquake and stability evaluation of the back scarp of the remnant slope. *Bull Eng Geol Environ* 78(3):2081–2092. <https://doi.org/10.1007/s10064-018-1233-6>
- Li H, Pel L, You Z, Smeulders D (2024) Stress-dependent instantaneous cohesion and friction angle for the Mohr-Coulomb criterion. *Int J Mech Sci* 283:109652. <https://doi.org/10.1016/j.ijmecsci>
- Ning YB, Zhang GC, Tang HM, Shen WC, Shen PW (2019) Process analysis of toppling failure on anti-dip rock slopes under seismic load in southwest China. *Rock Mech Rock Eng* 52(11):4439–4455. <https://doi.org/10.1007/s00603-019-01855-z>
- Pu XW, Wang LM, Wang P, Chai SF (2020) Study of shaking table test of seismic subsidence loess landslides induced by the coupling effect of earthquakes and rainfall. *Nat Hazards* 103(1):923–945. <https://doi.org/10.1007/s11069-020-04019-3>
- Peng JB, Wang SK, Wang QY, Zhuang JQ, Huang WL, Zhu XH, Leng YQ, Ma PH (2019) Distribution and genetic types of loess landslides in China. *J Asian Earth Sci* 170:329–350. <https://doi.org/10.1016/j.jseaes.2018.11.015>
- Qi SW, He JX, Zhan ZF (2022) A single surface slope effects on seismic response based on shaking table test and numerical simulation. *Eng Geol*. <https://doi.org/10.1016/j.enggeo.2022.106762>
- Shi WP, Zhang JW, Song DQ, Liu XL, Wang EZ, Zhao JJ (2024) Dynamic response characteristics and instability mechanism of high-steep bedding rock slope at the tunnel portal in high-intensity seismic region. *Rock Mech Rock Eng* 57(2):827–849. <https://doi.org/10.1007/s00603-023-03629-0>
- Song DQ, Che AL, Zhu RJ, Ge XR (2019) Natural frequency characteristics of rock masses containing a complex geological structure and their effects on the dynamic stability of slopes. *Rock Mech Rock Eng* 52(11):4457–4473. <https://doi.org/10.1007/s00603-019-01885-7>
- Song DQ, Liu XL, Huang J, Zhang JM (2021a) Energy-based analysis of seismic failure mechanism of a rock slope with discontinuities using Hilbert-Huang transform and marginal spectrum in the time-frequency domain. *Landslides* 18(1):105–123. <https://doi.org/10.1007/s10346-020-01491-7>
- Song DQ, Liu XL, Huang J, Zhang YF, Zhang JM, Nkwenti BN (2021b) Seismic cumulative failure effects on a reservoir bank slope with a complex geological structure considering plastic deformation characteristics using shaking table tests. *Eng Geol* 286:106085. <https://doi.org/10.1016/j.enggeo.2021.106085>
- Song DQ, Liu XL, Li B, Zhang JM, Bastos JJV (2020) Assessing the influence of a rapid water drawdown on the seismic response characteristics of a reservoir rock slope using time–frequency analysis. *Acta Geotech* 16:1281–1302. <https://doi.org/10.1007/s11440-020-01094-5>
- Su LJ, Li C, Zhang CL (2021) Large-scale shaking table tests on the seismic responses of soil slopes with various natural densities. *Soil Dyn Earthq Eng* 140:106409. <https://doi.org/10.1016/j.soildyn.2020.106409>
- Tao K, Dang WG (2023) Frictional behavior of quartz gouge during slide-hold-slide considering normal stress oscillation[J]. *Int J Coal Sci Technol* 10(3):34. <https://doi.org/10.1016/j.jrmge.2021.09.011>
- Tao K, Dang WG, Li YC (2023a) Frictional sliding of infilled planar granite fracture under oscillating normal stress. *Int J Min Sci Technol* 33(6):687–701. <https://doi.org/10.1016/j.ijmst.2022.12.001>
- Tao K, Dang WG, Liao X, Li XX (2023b) Experimental study on the slip evolution of planar fractures subjected to cyclic normal stress[J]. *Int J Coal Sci Technol* 10(4):67
- Verrucci L, Pagliaroli A, Lanzo G, Di Buccio F, Biasco AP, Cucci C (2022) Damping formulations for finite difference linear dynamic analyses: performance and practical recommendations. *Comput Geotech* 142:104568

- Wu ZJ, Zhao DY, Che AL, Chen DW, Liang C (2020a) Dynamic response characteristics and failure mode of slopes on the loess tableland using a shaking-table model test. *Landslides* 17(7):1561–1575. <https://doi.org/10.1007/s10346-020-01373-y>
- Wu ZJ, Zhang D, Wang S, Liang C, Zhao D (2020b) Dynamic-response characteristics and deformation evolution of loess slopes under seismic loads. *Eng Geol* 267:105507. <https://doi.org/10.1016/j.enggeo.2020.105507>
- Xin CL, Wang ZZ, Gao B (2018) Shaking table tests on seismic response and damage mode of tunnel linings in diverse tunnel-void interaction states. *Tunn Undergr Space Technol* 77:295–304. <https://doi.org/10.1016/j.tust.2018.03.010>
- Xin CL, Wang ZZ, Yu J (2020) The evaluation on shock absorption performance of buffer layer around the cross section of tunnel lining. *Soil Dyn Earthq Eng* 131:106032. <https://doi.org/10.1016/j.soildyn.2020.106032>
- Xin CL, Wang ZZ, Zhou JM, Gao B (2019) Shaking table tests on seismic behavior of polypropylene fiber reinforced concrete tunnel lining. *Tunn Undergr Space Technol* 88:1–15. <https://doi.org/10.1016/j.tust.2019.02.019>
- Xin CL, Li WH, Wang Z, Feng WK, Hajirasouliha I, Yu XY (2024) Shaking table tests on the stability of dip and anti-dip rock slopes with structural planes induced by seismic motions. *Eng Geol* 341:107707
- Xu M, Tang YF, Liu XS, Yang HQ, Luo B (2018) A shaking table model test on a rock slope anchored with adaptive anchor cables. *Int J Rock Mech Min Sci* 112:201–208. <https://doi.org/10.1016/j.ijrmms.2018.10.021>
- Yin JH, Chen J, Xu XW, Wang XL, Zheng YG (2010) The characteristics of the landslides triggered by the Wenchuan Ms 8.0 earthquake from Anxian to Beichuan. *J Asian Earth Sci* 37(5):452–459. <https://doi.org/10.1016/j.jseae.2009.12.002>
- Zhang CL, Miao SS, Su LJ (2022) Seismic behaviour of granular slope under railway embankment in large-scale shaking table test. *Eng Geol* 305:106714. <https://doi.org/10.1016/j.enggeo.2022.106714>
- Zhou HX, Che AL, Zhu RJ (2022) Damage evolution of rock slopes under seismic motions using shaking table test. *Rock Mech Rock Eng* 55(8):4979–4997. <https://doi.org/10.1016/j.enggeo.2018.08.011>

Publisher's Note Springer Nature remains neutral with regard to jurisdictional claims in published maps and institutional affiliations.